Bioactive Materials 6 (2021) 4654–4669

Contents lists available at ScienceDirect

Bioactive Materials

journal homepage: www.sciencedirect.com/journal/bioactive-materials

Improving in vitro and in vivo corrosion resistance and biocompatibility of Mg–1Zn–1Sn alloys by microalloying with Sr

Yafeng Wen [a], Qingshan Liu [b], Jingfeng Wang [b,**], Qiming Yang [a], Weikang Zhao [a], Bo Qiao [a], Yuling Li [c], Dianming Jiang [d,*]

[a] Department of Orthopaedics, The First Affiliated Hospital of Chongqing Medical University, Chongqing, 400042, People's Republic of China
[b] National Engineering Research Center for Magnesium Alloys, College of Materials Science and Engineering, Chongqing University, Chongqing, 400044, People's Republic of China
[c] Department of Orthopaedics, Affiliated Hospital of North Sichuan Medical College, No. 63 Wenhua Road, Nanchong City, Sichuan Province, 637000, People's Republic of China
[d] The Third Affiliated Hospital of Chongqing Medical University, No.1 Shuanghu Road, Yubei District, Chongqing, 401120, People's Republic of China

ARTICLE INFO

Keywords:
Magnesium alloy
Strontium
Biodegradable
Biocompatibility
Corrosion resistance

ABSTRACT

Magnesium (Mg) and its alloys have attracted attention as potential biodegradable materials in orthopedics due to their mechanical and physical properties, which are compatible with those of human bone. However, the effect of the mismatch between the rapid material degradation and fracture healing caused by the adverse effect of hydrogen (H_2), which is generated during degradation, on surrounding bone tissue has severely restricted the application of Mg and its alloys. Thus, the development of new Mg alloys to achieve ideal degradation rates, H_2 evolution and mechanical properties is necessary. Herein, a novel Mg–1Zn–1Sn-xSr (x = 0, 0.2, 0.4, and 0.6 wt%) quaternary alloy was developed, and the microstructure, mechanical properties, corrosion behavior and biocompatibility in vitro/vivo were investigated. The results demonstrated that a minor amount of strontium (Sr) (0.2 wt %) enhanced the corrosion resistance and mechanical properties of Mg–1Zn–1Sn alloy through grain refinement and second phase strengthening. Simultaneously, due to the high hydrogen overpotential of tin (Sn), the H_2 release of the alloys was significantly reduced. Furthermore, Sr-containing Mg–1Zn–1Sn-based alloys significantly enhanced the viability, adhesion and spreading of MC3T3-E1 cells in vitro due to their unique biological activity and the ability to spontaneously form a network structure layer with micro/nanotopography. A low corrosion rate and improved biocompatibility were also maintained in a rat subcutaneous implantation model. However, excessive Sr (>0.2 wt %) led to a microgalvanic reaction and accelerated corrosion and H_2 evolution. Considering the corrosion resistance, H_2 evolution, mechanical properties and biocompatibility in vitro and in vivo, Mg–1Zn–1Sn-0.2Sr alloy has tremendous potential for clinical applications.

1. Introduction

Since the early 2000s, Mg-based biodegradable metals have developed rapidly and received widespread attention because of their appropriate mechanical properties, good biocompatibility, excellent osseointegration performance and unique biodegradability [1–4]. Mg alloys have physicochemical properties similar to those of traditional metal materials, such as excellent strength, plasticity and workability, which are appealing for orthopedic implant applications. Moreover, their density and elastic modulus are very close to those of human cortical bone [5], which are much better than those of traditional metal materials and can effectively eliminate/decrease the stress shielding effect and resulting osteoporosis [6]. In addition, their unique biodegradability allows secondary operations to be avoided and greatly eases the pain and financial burden of patients, making them excellent candidates for orthopedic implants [7]. In 2013, MAGNEZIX® (MgYReZr) screw fabricated by Syntellix AG (Germany) received the CE mark and became the first Class III medical device made of Mg alloy approved for

Peer review under responsibility of KeAi Communications Co., Ltd.
* Corresponding author.
** Corresponding author.
E-mail addresses: jfwang@cqu.edu.cn (J. Wang), 201296@hospital.cqmu.edu.cn (D. Jiang).

https://doi.org/10.1016/j.bioactmat.2021.04.043
Received 15 October 2020; Received in revised form 22 April 2021; Accepted 23 April 2021

Table 1
Nominal and actual compositions of the Mg–Zn–Sn–Sr alloys (wt. %).

Nominal composition	Actual composition						
	Zn	Sn	Sr	Fe	Si	Ni	Mg
Mg–1Zn–1Sn	1.11	1.17	0	<0.01	<0.01	<0.001	Balance
Mg–1Zn–1Sn-0.2Sr	1.10	1.14	0.13	<0.01	<0.01	<0.001	Balance
Mg–1Zn–1Sn-0.4Sr	1.06	1.17	0.38	<0.01	<0.01	<0.001	Balance
Mg–1Zn–1Sn-0.6Sr	1.11	1.05	0.51	<0.01	<0.01	<0.001	Balance

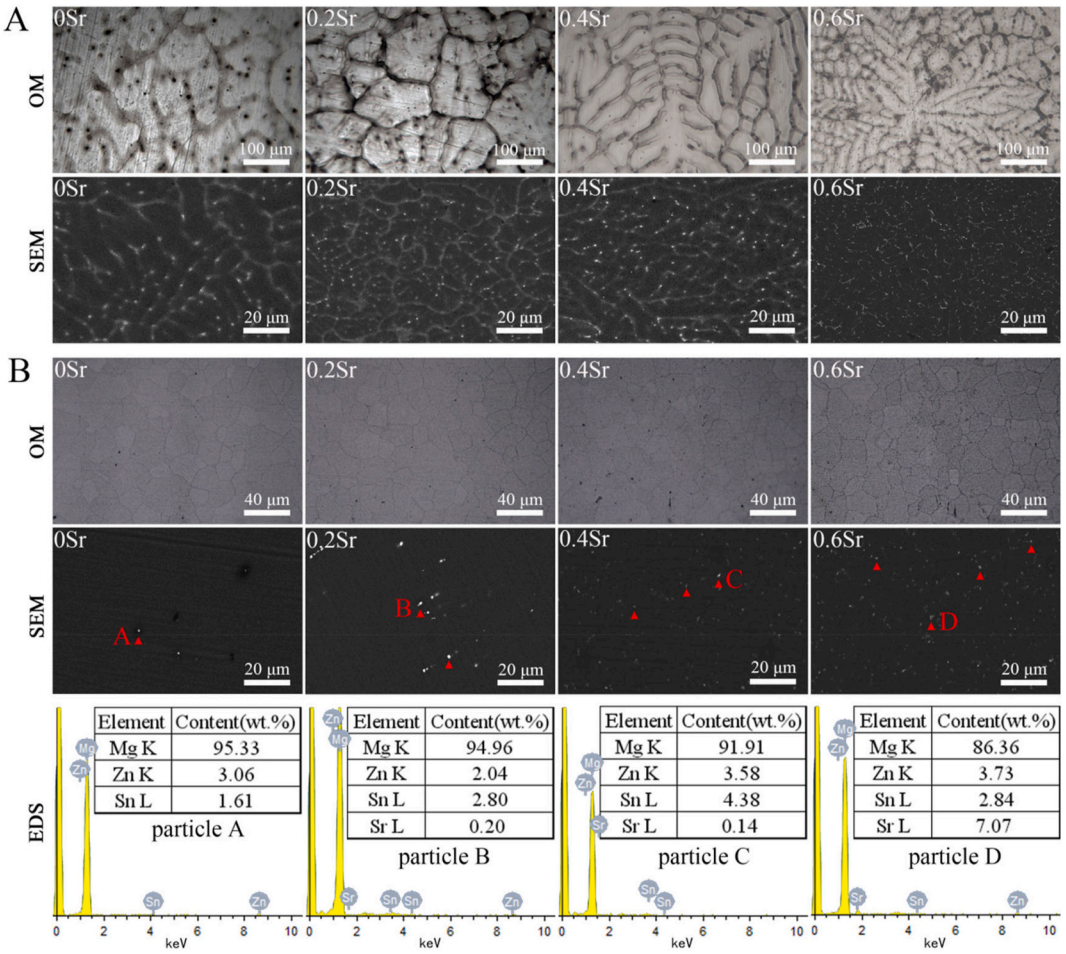

Fig. 1. (A) Optical microstructure and SEM images of the as-cast and (B) as-extruded Mg–1Zn–1Sn-xSr alloys (x = 0, 0.2, 0.4, and 0.6 wt %) and corresponding EDS results. The red triangle indicates the second phase.

clinical use [8]. The first clinically proven Mg-based biodegradable stent received CE mark approval in 2016 [9]. However, due to the presence of rare earth (RE) metal elements, their long-term biosafty remains controversial.

From a clinical viewpoint, the corrosion rate of ideal orthopedic Mg implants needs to be less than 0.5 mm year^{-1}, the strength must be higher than 200 MPa and the elongation should be greater than 10% [5]. It is critical for implants to maintain mechanical integrity for 90–180 days [10,11] and release nontoxic species, such as hydroxide ions, hydrogen gas, and metal ions [10,12]. Other biological concerns, such as cell attachment, biocompatibility, and osteogenic activity, must also be considered. To date, a large number of Mg-based alloys have been developed. Binary Mg alloys with deeper research include Mg-Zn [13], Mg-Ca [14], Mg-Sr [15], Mg-Mn [13], Mg-Si [16], and ternary or multicomponent alloys developed on the basis of them.

Our previous research found that Mg–Zn–Sn ternary alloys have great potential in the field of orthopedic implants due to their excellent mechanical properties, biocompatibility and low H_2 evolution in vitro [17,18]; however, their corrosion resistance in vivo still needs to be improved. Sr is an essential trace element with unique chemical and biological properties: (1) Sr has excellent biological safety and can be absorbed and excreted by the human body [2]; (2) Appropriate amount of Sr can improve the corrosion resistance of Mg alloys by grain refinement [19]; (3) Sr can enhance mechanics of Mg alloys by solution strengthening effect [20]; (4) Sr can promote the proliferation of pre-osteoblasts, osteoblast differentiation, type I collagen synthesis and bone matrix mineralization while inhibiting the differentiation and activation of osteoclasts [21]. Clinically, oral strontium salt (strontium ranelate) can increase bone mass, reduce the chance of fracture, and treat patients with osteoporosis [22]. An appropriate amount of Sr incorporated in Mg can effectively improve the mechanical strength, corrosion resistance, biocompatibility and antibacterial properties of Mg alloys [19,23,24].

In the present study, four Mg–1Zn–1Sn-xSr quaternary alloys (x = 0, 0.2, 0.4, and 0.6 wt %) were prepared. This paper presents early insights

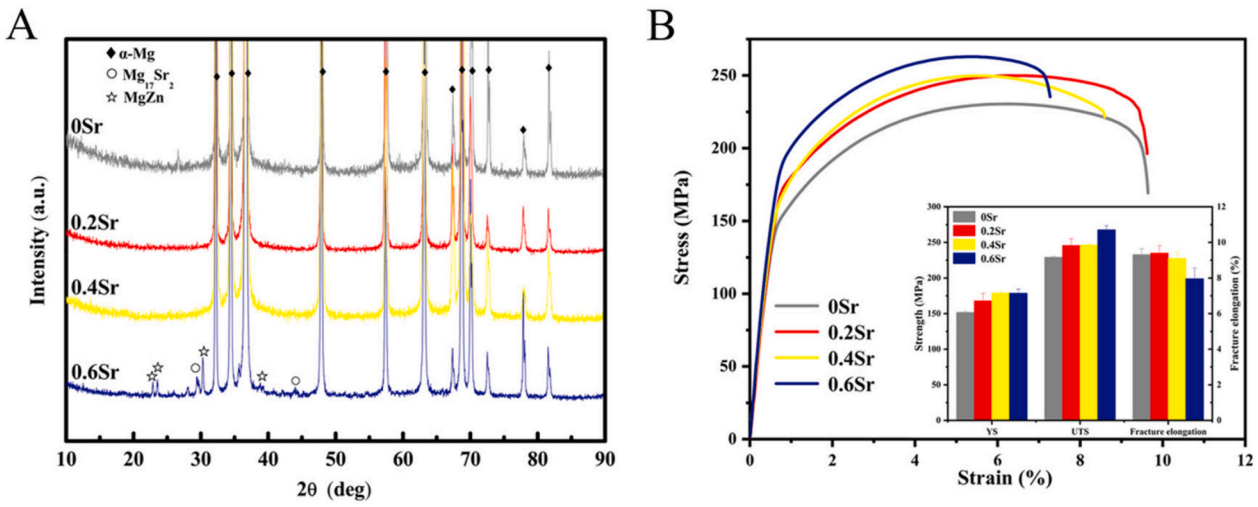

Fig. 2. (A)XRD, (B) YS, UTS and elongation values of the as-extruded Mg–1Zn–1Sn-xSr alloys.

Table 2
Mechanical properties of the as-extruded alloys with different Sr additions.

Materials	Alloy state	Mechanical properties			refs.
		Ultimate tensile strength (MPa)	Yield strength (MPa)	Elongation (%)	
Cortical bone		35–283	105–114	1.07–2.00	[36]
Cancellous bone		1.5–38	–	–	[36]
Mg–1Zn–1Sn	As-extruded	229 ± 1	151 ± 1	9.0 ± 0.9	present study
Mg–1Zn–1Sn-0.2Sr	As-extruded	245 ± 8	168 ± 8	9.0 ± 0.4	present study
Mg–1Zn–1Sn-0.4Sr	As-extruded	246 ± 2	179 ± 3	9.0 ± 0.5	present study
Mg–1Zn–1Sn-0.6Sr	As-extruded	268 ± 6	178 ± 5	8.0 ± 0.7	present study
Mg–1Zn–1Mn-xSr	As-extruded	~280	~241	~18	[34]
Mg-3.2Zn-0.3Sr	As-extruded	278 ± 5	187 ± 4	19	[35]
Mg–1Zn-xSr	As-extruded	~249	~130	~12	[33]

into the microstructure, mechanical properties, corrosion behavior, and in vitro/vivo biocompatibility of Mg–1Zn–1Sn-xSr alloys.

2. Materials and methods

2.1. Preparation of the Mg–1Zn–1Sn-xSr alloys

High-purity Mg (99.98 wt %), high-purity Zn (99.99 wt %), high-purity Sn (99.99 wt %) and Mg-15 wt % Sr master alloys were used to prepare the Mg–1Zn–1Sn-xSr (x = 0, 0.2, 0.4 and 0.6 wt %) alloys. The alloys were smelted in an electric resistance furnace under the protection of an SF_6 and CO_2 gas (SF_6: CO_2 = 1 : 99) mixture in a graphite crucible to obtain the ingot casting. After homogenization treatment at 500 °C for 6 h, the ingot casting was extruded at 280 °C with an extrusion ratio of 28 : 1 [25,26]. Subsequently, the as-extruded Mg–1Zn–1Sn-xSr ingots were cut into sheets, and commercial pure-Mg (p-Mg) was used as a reference. The as-extruded Mg–1Zn–1Sn-xSr sheets were cut into ϕ15 mm × 1 mm wafers and 5 mm × 5 mm × 1 mm squares for characterization, electrochemical tests, and in vitro/vivo experiments. All samples were polished with SiC abrasive paper up to 1200 grit, ultrasonically cleaned for 15 min in separate baths of acetone and ethanol, individually weighed and sterilized with ethylene oxide.

2.2. Microstructure analysis and mechanical testing

The microstructures of the samples were examined using optical microscopy (OM, OLYMPUS, Japan) and scanning electron microscopy (SEM, Vega III LMH) equipped with energy dispersive X-ray spectroscopy (EDS). Furthermore, the phases of the Mg–1Zn–1Sn-xSr alloys were detected by X-ray diffraction (XRD, Rigaku D/max/2500 PC, Japan) with CuKα radiation and a scanning speed of 5°/min. The compositions of the alloys were determined by using inductively coupled plasma optical emission spectrometry (ICP-OES, PerkinElmer, Optima 8000). The actual chemical compositions of the Mg–1Zn–1Sn-xSr alloys are listed in Table 1.

According to the specifications of GB/T16865-2013, tensile specimens with a gauge length of 25 mm and a diameter of 6 mm were tested on a tensile testing machine (CTM-5106, China) in air at a cross head speed of 2 mm/min at room temperature.

2.3. Electrochemical test

Potentiodynamic polarization (PDP) and electrochemical impedance spectroscopy (EIS) tests were carried out on an electrochemical workstation (CHI600C, China) in Hank's balanced salt solution (HBSS) (Table S1). Specific details pertaining to the preparation of the working electrode are given elsewhere [27]. Briefly, polished Mg–1Zn–1Sn-xSr samples embedded in epoxy resin to expose only a 1 cm^2 area surface were used as the working electrode. Platinum foil was used as the counter electrode, and a saturated calomel electrode was used as a reference. Before the potentiodynamic polarization test, the sample was immersed in HBSS (37.0 ± 0.1 °C) for 1200 s and reached the stability of the open-circuit potential. Afterwards, a PDP curve was generated at a scanning rate of 1 mV s^{-1} for all the measurements. The corrosion potential (E_{corr}), corrosion current density (i_{corr}) and polarization resistance (Rp) were calculated according to Tafel extrapolation. The EIS tests were carried out using a 10 mV root-mean-square perturbation from 100 kHz to 100 mHz. The EIS results were fitted via ZView software.

2.4. Immersion testing

The samples were immersed in HBSS at 37 ± 1 °C for 7 days. According to ASTM-G31-72 [28], the ratio of the sample surface area to the volume of HBSS was 20 ml/cm^2. The pH value during immersion was monitored by a pH meter (PHS–3C). For the H_2 evolution test, the ratio

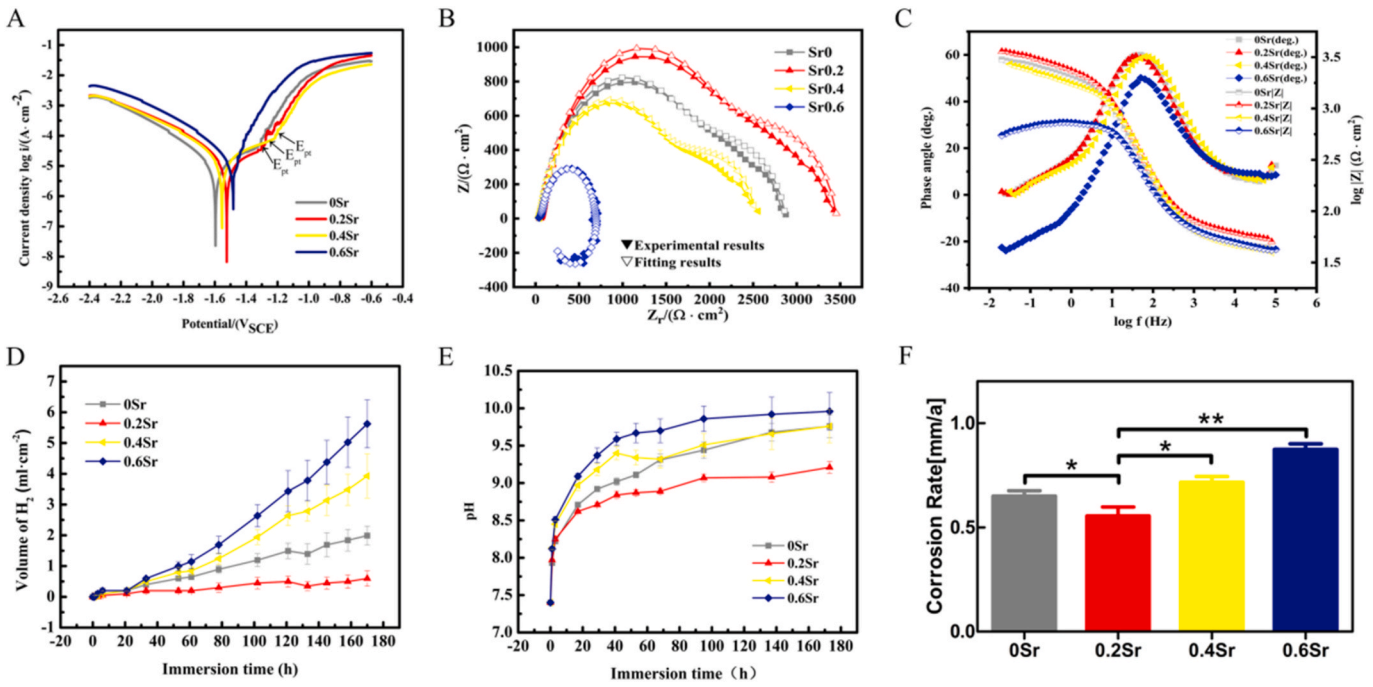

Fig. 3. (A) Potentiodynamic polarization curves of the Mg–1Zn–1Sn-xSr alloys in HBSS, (B) Nyquist plot, (C) |z|-logf plot and θ-logf plot of EIS spectrum of the Mg–1Zn–1Sn-xSr alloys, (D) H_2 evolution, (E) changes of pH value and (F) corrosion rate of the Mg–1Zn–1Sn-xSr alloys in HBSS at 37 °C for 7 days.

Table 3
Electrochemical parameters of the Mg–1Zn–1Sn-xSr alloys obtained from polarization tests.

Sample	E_{corr} (V)	I_{corr} (μA. cm^{-2})	E_{pt} (V)	R_P (Ω. cm^2)	R_t (Ω. cm^2)	CR (mm/a)
Mg–1Zn–1Sn	−1.59	7.36	−1.31	4647.54	1224	0.24
Mg–1Zn–1Sn-0.2Sr	−1.55	6.55	−1.25	5619.02	1304	0.18
Mg–1Zn–1Sn-0.4Sr	−1.56	12.24	−1.21	3546.91	1018	0.31
Mg–1Zn–1Sn-0.6Sr	−1.48	15.74	–	1675.34	540	0.39

of surface area to solution volume was 150 ml/cm^2 [20]. The surface topographies of the alloys after immersion were observed by SEM. The surface chemistry was characterized by XRD, EDS and X-ray photoelectron spectroscopy(XPS, Thermo Fisher, USA). The mass loss was also measured after removing the corrosion products in chromic acid. Then, the mass loss data were converted to a corrosion rate using the following equation:

CR =KW/ADT [28,29]

where the constant K is 8.76 × 10^4, W is the mass loss (g), A is the surface area exposed to solution (cm^2), D is the density of the material (g/cm^3) and T is the immersion time (h). At least three samples were tested in each group.

2.5. In vitro cell testing

2.5.1. Preparation of the extraction

The extraction was prepared according to a reference [30]. Briefly, samples were immersed in Dulbecco's modified Eagle's medium (DMEM, HyClone, USA) supplemented with 10% (v/v) fetal bovine serum (FBS, Gibco, USA) for 72 h under standard cell culture conditions (37 °C, 5% CO_2, and 95% humidity) with a ratio of sample mass to medium volume of 0.2 g/ml.

2.5.2. Cell culture

The murine calvarial preosteoblasts (MC3T3-E1) were devoted to cytocompatibility evaluations of all samples. To more closely mimic in vivo conditions where the circulatory system regularly removes soluble degradation products from the local implantation site, incubation intervals were set to 24 h.

2.5.3. Cell viability and cytotoxicity evaluation

A cell counting kit-8 (CCK-8) assay was adopted to evaluate the cell viability. Specifically, cells at a density of 1 × 10^4 cells/well were cultured in a 96-well plate for 24 h. Next, the medium was replaced with the extracts, with normal culture medium as the negative control. After incubating for 24, 48, and 72 h, 20 μl of CCK-8 assay reagent was added into each well and incubated for 1 h. Then, the absorbance was measured by a microplate spectrophotometer (Thermo Scientific, USA) at a wavelength of 450 nm.

The live/dead cell assay was performed according to the protocol from the manufacturer (BestBio, China). In brief, cells were stained with 200 μl of a 1:10000 dilution of calcein-AM solution for 30 min and 200 μl of a 1:5000 dilution of PI solution for 5 min. Finally, after examination by fluorescence microscopy (Zeiss, Germany), the viable cells combined with calcein-AM were stained green, whereas dead cells combined with PI were stained red.

2.5.4. Cell apoptosis and cycle

To further evaluate the effect of extracts on cell apoptosis and cell cycle progression [2], the cells were treated with the extracts for 48 h, washed three times with phosphate buffered saline (PBS), centrifuged, and fixed with precooled 75% ethanol at 4 °C for 24 h. Then, the cells were resuspended in a mixture containing 100 μL of PBS and 200 μL of propidium iodide (PI) solution and protected from light for 20 min. Detection was performed by flow cytometry (CytoFLEX, Beckman-Coulter, USA). To detect apoptosis, the cells were stained with FITC-Annexin V and PI (BD, USA) according to the protocol from the manufacturer and analyzed by flow cytometry (CytoFLEX, Beckman-Coulter, USA) [31].

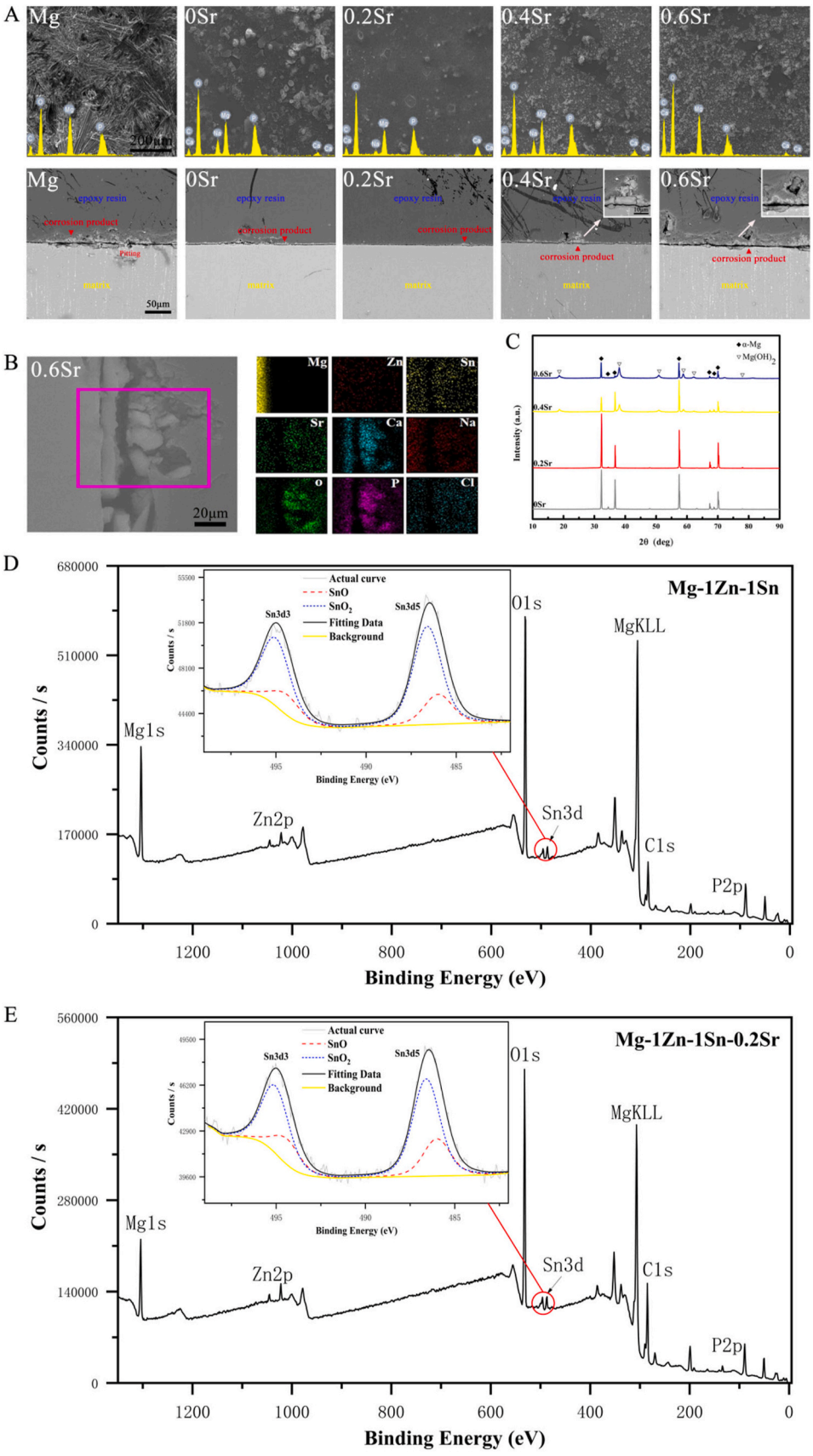

Fig. 4. (A) Surface topographies (scale bar = 200 μm), element distributions, and morphologies of corrosion products on the cross section (scale bar = 50 μm) of Mg–1Zn–1Sn-xSr alloys after 5 days of immersion in HBSS. Insets in (A) were taken at 2000 original magnification with scale bar = 10 μm for all images. (B) SEM-EDS composite image of cross-sectional morphologies of Mg–1Zn–1Sn-0.6Sr alloy immersed for 5 days in HBSS at 37 °C; scale bar = 20 μm. (C) XRD patterns of Mg–1Zn–1Sn-xSr alloys immersed for 5 days in HBSS. XPS surface analysis of survey and detailed Sn3d of (D) Mg–1Zn–1Sn and (E) Mg–1Zn–1Sn-0.2Sr alloys after 3 h immersion.

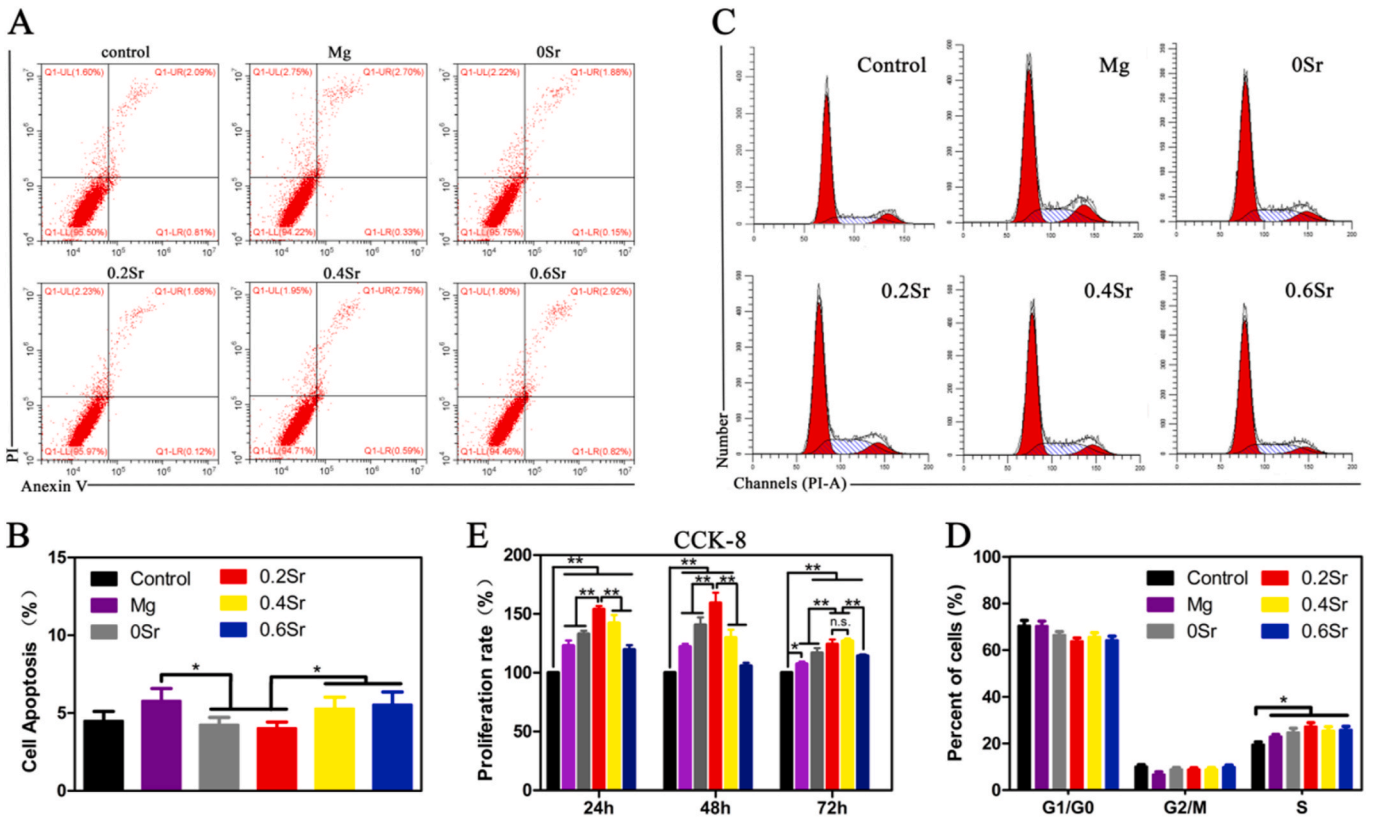

Fig. 5. (A,B) Cell apoptosis and (C,D) cycle results after coculture with p-Mg, Mg–1Zn–1Sn-xSr alloy extracts and DMEM control for 48 h. (E) Cell viability of MC3T3-E1 after coculture with p-Mg, Mg–1Zn–1Sn-xSr alloy extracts and DMEM control for 24, 48 and 72 h. Values are the mean ± SD, n = 3. *p < 0.05, and **p < 0.01.

2.5.5. Cell adhesion and morphology

The adhesion and morphologies of the actin cytoskeleton of cells cocultured with samples after 24, 48 and 72 h were observed by confocal laser scanning microscopy (CLSM). Briefly, cells were washed with PBS, fixed with 4% paraformaldehyde, and permeabilized with 0.1% Triton X-100. Nuclei were stained with 4′,6-diamidino-2-phenylindole dilactate (DAPI; Invitrogen), and F-actins were stained with Actin-Tracker Green (Beyotime Biotechnology, Shanghai, China). Images of cells on the glass and surface of samples were observed and captured by using CLSM (Zeiss, Germany).

The spread of cells on the surface of samples was examined by SEM. In brief, the samples were immersed in 2.5% glutaraldehyde for 15 min at room temperature. Next, samples were dehydrated in graded ethanol (10, 30, 50, 70, 90, and 100% ethanol sequentially; 10 min each) and then immersed in graded tertiary butanol (50, 70, 90, 95, 100 and 100% tertiary butanol sequentially; 5 min each). Finally, after air-drying and gold sputtering, the morphologies of the attached cells were observed by SEM (Zeiss, Germany).

2.5.6. In vitro degradation of Mg–1Zn–1Sn-xSr alloys in DMEM

The in vitro degradation of the Mg–1Zn–1Sn-xSr alloys and p-Mg after 24, 48 and 72 h of culture was evaluated through measurements of the pH and ionic concentrations of the collected media, and H_2 evolution in the media was also observed. The pH of the medium was measured immediately after collection as well as the concentrations of metal ions including Mg, Zn, Sn and Sr.

2.6. In vivo animal studies

2.6.1. Animal model and experimental design

All animal experiments were approved by the Animal Care and Experiment Committee of the First Affiliated Hospital of Chongqing Medical University and the Animal Ethics Committee of the First Affiliated Hospital of Chongqing Medical University (No: 20187801). Twelve Sprague-Dawley (SD) rats (12 weeks old) were randomly assigned to four groups (control, 7-day, 15-day and 30-day groups, n = 3). All rats were generally anesthetized with pentobarbital sodium (30 mg/kg) by intraperitoneal injection. Four independent incisions parallel to the spine in a longitudinal row on both sides of the spine were made on the back of each rat [32]. One sample was implanted in a subcutaneous pocket through one incision. Each rat carried two parallel samples. The control group only made skin incisions without implanting samples.

2.6.2. Blood testing

One milliliter of blood was collected from each rat before and at 3, 7, 15 and 30 days after implantation. The hematological parameters, including aspartate aminotransferase (AST), alanine aminotransferase (ALT), creatinine (CREA), blood urea nitrogen (BUN) and serum magnesium ion concentration, were measured using a hematological autoanalyzer (IDEXX Catalyst One, USA).

2.6.3. Histological evaluations postsurgery

Rats were sacrificed on the 7th, 15th and 30th days after implantation, subcutaneous tissues containing samples and vital organs were harvested. Next, the subcutaneous tissues and vital organs (such as the heart, liver, spleen and kidney) were fixed in 4% paraformaldehyde and dehydrated before being embedded in paraffin. Histological sections were stained with hematoxylin-eosin (H&E). Images were obtained by OM (Zeiss, Germany). A chromic acid solution (200 g of CrO_3 and 10 g of $AgNO_3$ per liter of water) was used to clean the samples, and the mass loss was measured by an electronic balance (AUW120D, Japan). The changes in the surface topography were characterized by an optical camera.

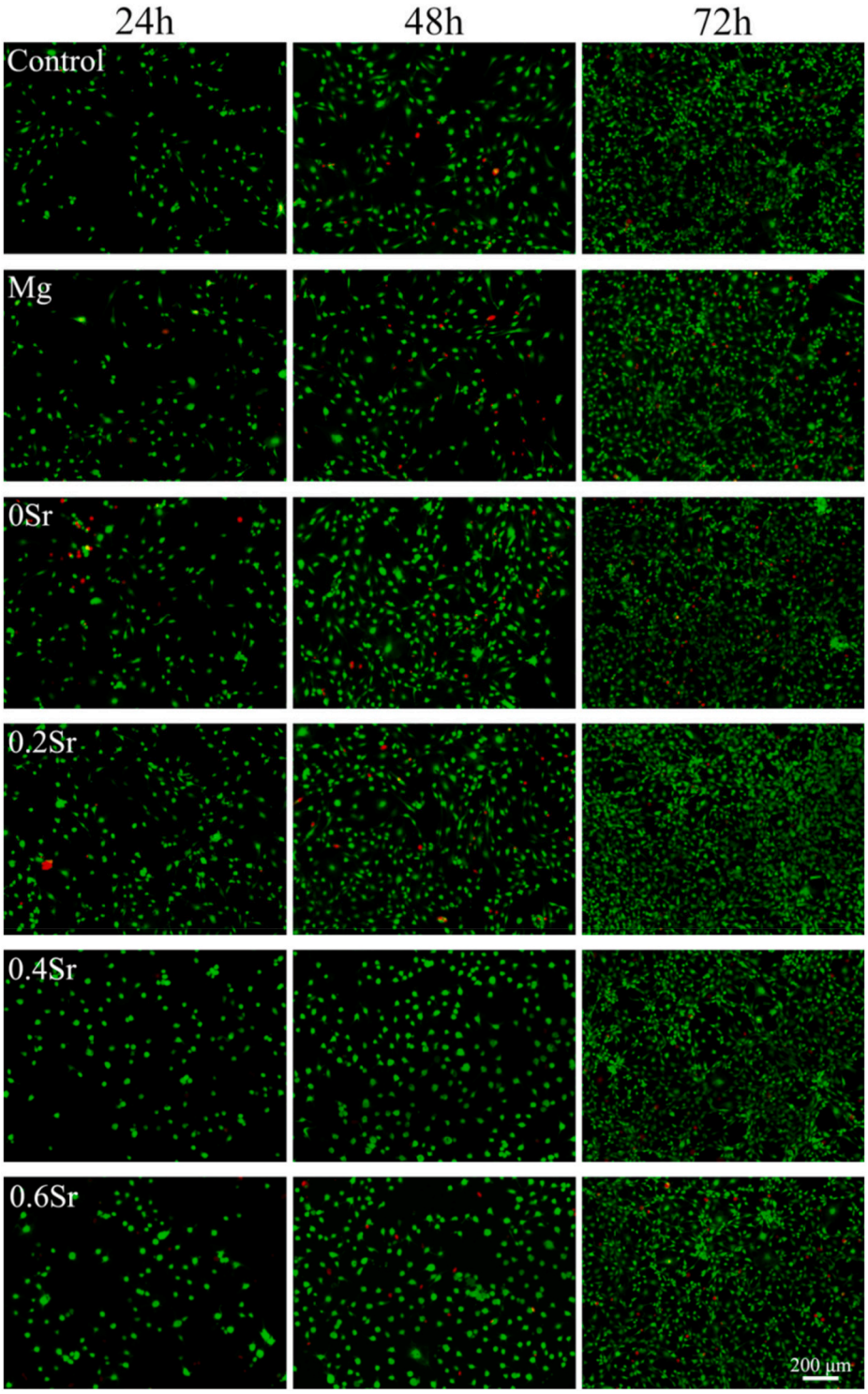

Fig. 6. Live/dead staining of MC3T3-E1 cells after coculture with p-Mg, Mg–1Zn–1Sn-xSr alloy extracts and DMEM control for 24, 48 and 72 h; scale bar = 200 μm for all images.

2.7. Statistical analyses

All continuous data are presented as the mean ± standard deviation, and the statistical significance of differences between groups was determined by using a single factor one-way analysis of variance (ANOVA) post hoc test where $p < 0.05$ was considered statistically significant. The statistical analyses were performed with SPSS software (Version 17.0).

3. Results

3.1. Microstructure and mechanical properties

Fig. 1 displays the OM and SEM images of the as-cast and as-extruded Mg–1Zn–1Sn-xSr alloys. The grain size gradually decreased in the as-cast Mg–1Zn–1Sn-xSr alloys as the content of Sr increased, and the 0.4Sr and 0.6Sr alloys showed typical dendritic structures and segregated eutectic characteristics. Some point-like second phases

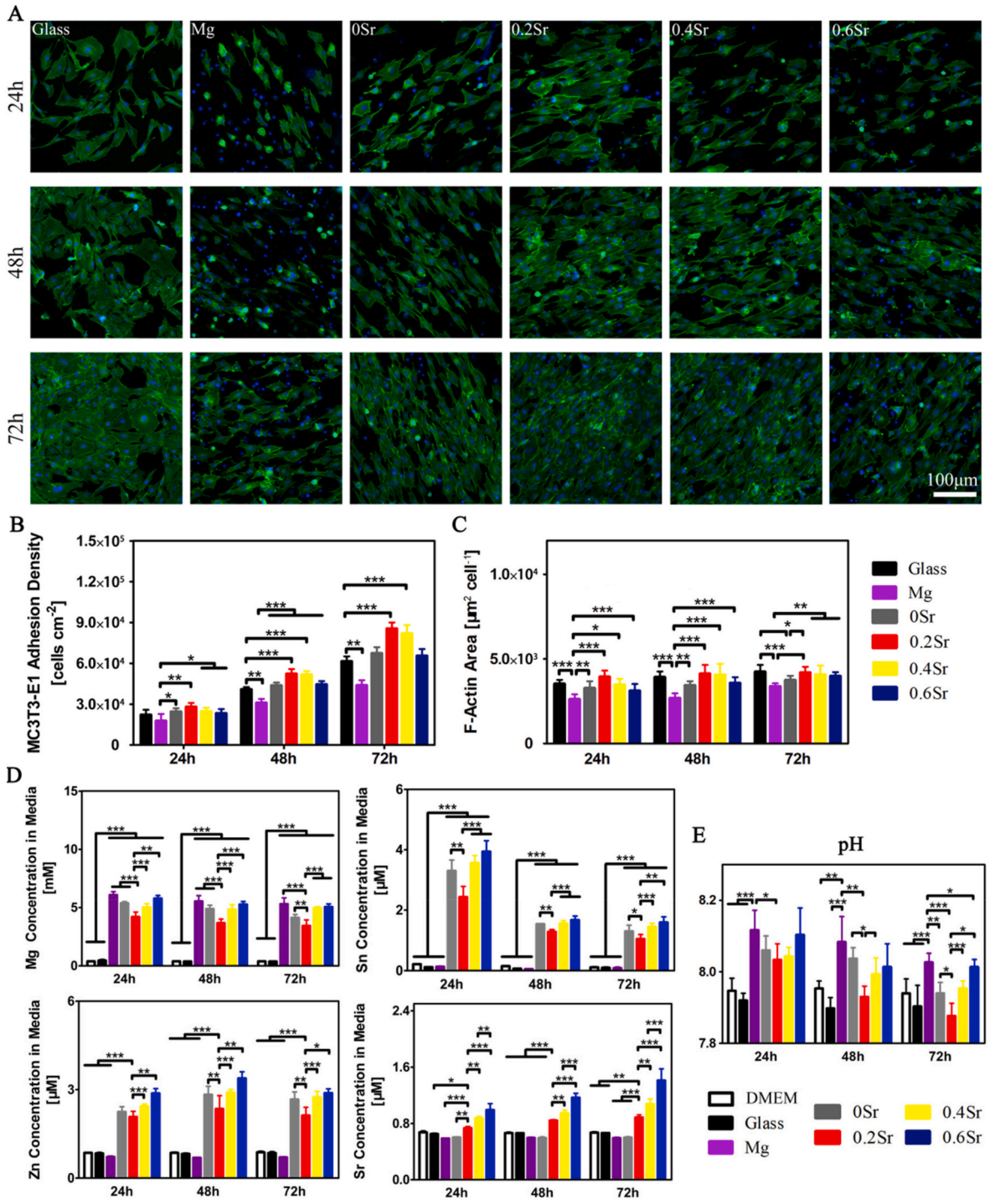

Fig. 7. (A) Fluorescence images of MC3T3-E1 adhered to the surface of the Mg–1Zn–1Sn-xSr alloys (x = 0, 0.2, 0.4, and 0.6 wt %), p-Mg control and glass reference after coculture for 24, 48 and 72 h. Blue indicates nuclei, and green indicates F-actin (cytoskeleton). The scale bar = 100 μm for all images. (B) Cell adhesion density on the sample surface. (C) Average F-actin area of MC3T3-E1 cells on the sample surface. (D) Mg, Zn, Sn and Sr ion concentrations, respectively, in culture medium incubated with the samples during a 72 h period. (E) pH values of culture medium incubated with samples during a 72 h period. Values are the mean ± SD, n = 3. *p < 0.05, **p < 0.01 and ***p < 0.001.

precipitated in the grains. The results showed that the addition of a minor amount of Sr had a remarkable refinement effect on the microstructure of the as-cast alloys [19,31]. Compared with that for the as-cast alloys, the as-extruded alloys had a finer microstructure. The SEM images of the as-cast and as-extruded alloys show that the second phase (white particles) distributed in the matrix increased randomly with increasing Sr content. To determine the composition of the second phase, EDS was used to analyze the four marked points (A, B, C, and D) in the as-extruded alloys and it was confirmed that the Sr was successfully incorporated into the Mg–1Zn–1Sn-based system.

Fig. 2 shows the corresponding XRD patterns and mechanical results of the as-extruded Mg–1Zn–1Sn-xSr alloys. The mechanical properties of certain Sr-containing alloys [33–35] and natural bone [36] are summarized in Table 2. Only peaks corresponding to α-Mg phase were found in the XRD patterns for 0Sr, 0.2Sr and 0.4Sr alloys probably due to the low volume fractions of the second phase. The $Mg_{17}Sr_2$ peaks could only

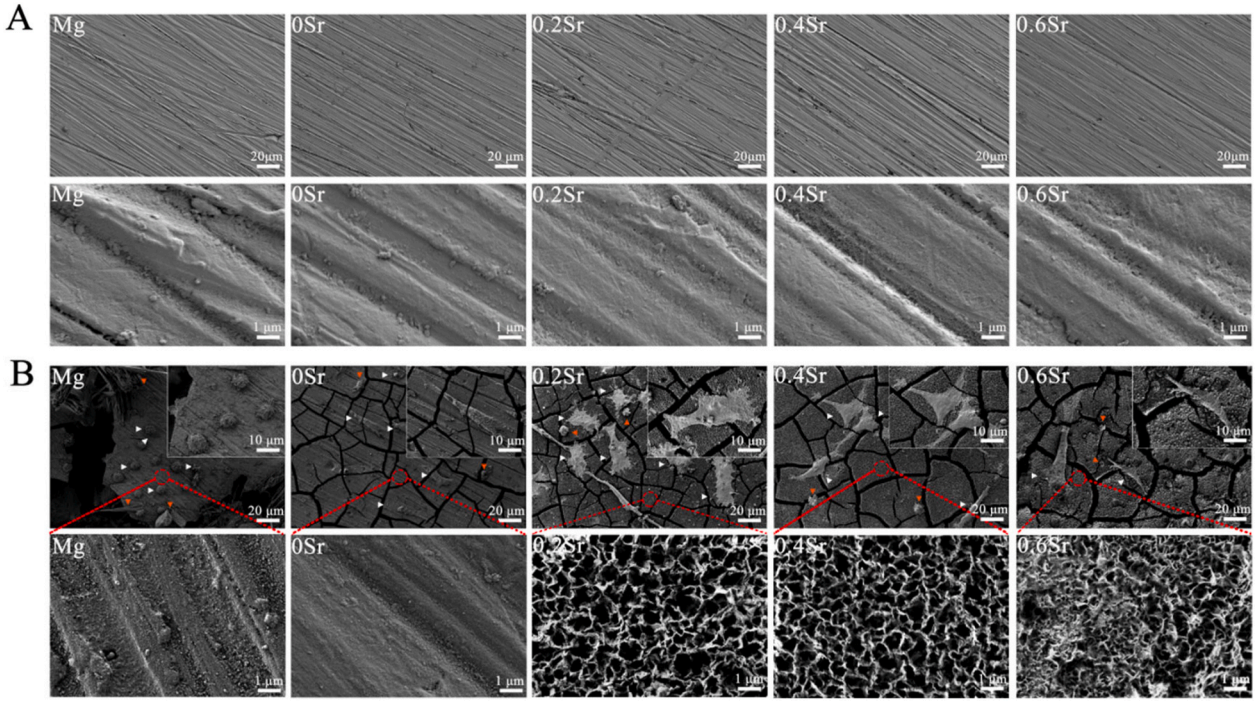

Fig. 8. (A) SEM images of Mg–1Zn–1Sn-xSr alloys and p-Mg surfaces before contact with the medium. (B) Morphology of MC3T3-E1 cells adhered to the surface of Mg–1Zn–1Sn-xSr alloys and p-Mg after coculture for 24 h. White triangle indicates cells, red triangle indicates degradation products.

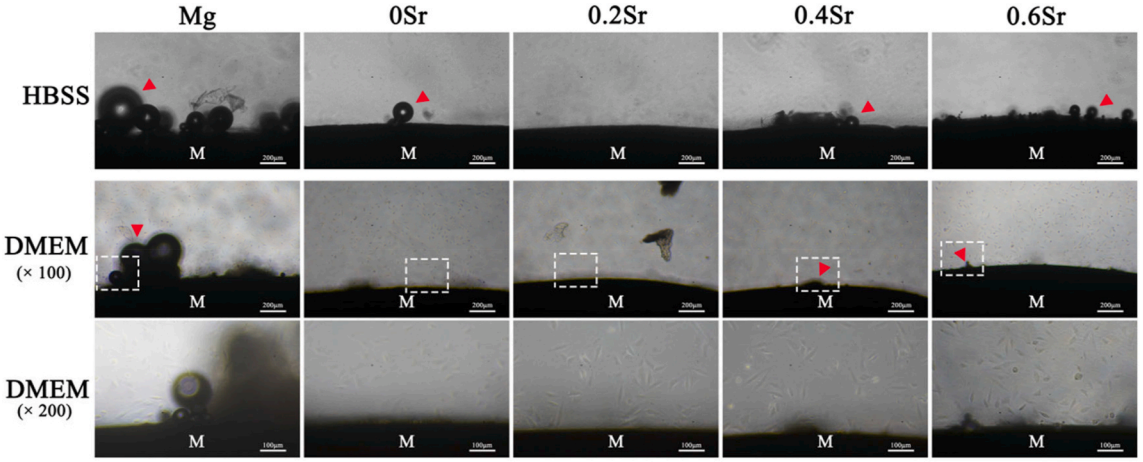

Fig. 9. The H_2 evolution of p-Mg and Mg–1Zn–1Sn-xSr alloys immersed in HBSS solution and cocultured with the MC3T3-E1 cells for 48 h. The scale bar = 200 μm. The dotted boxes were taken at 100 times the original magnification with a scale bar = 100 μm. The red arrow indicates H_2 bubbles.

be detected in the 0.6Sr alloy. The ultimate tensile strength (UTS) and yield strength (YS) of the as-extruded Mg–1Zn–1Sn-xSr alloys increased gradually with increasing Sr content from 0 to 0.6 wt %. When the content of Sr increased from 0 to 0.4 wt %, the fracture elongation (Ef) of the alloys was in the range from 9 ± 0.9–9 ± 0.4% and had no obvious downward trend. However, when the content of Sr increased to 0.6 wt %, the Ef was significantly reduced to 8%. After immersing all samples in HBSS for 20 days, the mechanical properties of 0.2Sr lost 20%, while 0.6Sr lost up to 50% (Fig. S1 and Table S2).

3.2. Corrosion behavior

The polarization curves and EIS results are presented in Fig. 3A, B and C, and the data are exhibited in Table 3. The E_{corr} gradually increases with increasing Sr content, the 0Sr, 0.2Sr and 0.4Sr alloys exhibited lower i_{corr} and higher R_p values than the 0.6Sr alloys. When the Sr content was less than 0.4 wt %, the polarization curves had similar characteristics; in particular, there was a breakdown potential (E_{pt}) near the potential of −1.2 V for the three alloys, which indicates that a protective film formed on the alloy surface, but when the Sr content was 0.6 wt %, a breakdown potential did not exist. The 0.2Sr alloy had the largest loop in the Nyquist plots, demonstrating a corrosion resistance that was superior to that of the other alloys. Moreover, 0.6Sr exhibited the smallest loop, indicating its poor corrosion resistance. The equivalent circuit for Mg–1Zn–1Sn-xSr alloys was shown in Fig. S2. R_t is the charge transfer resistance, which refers to the impedance of the corrosion reaction and the fitted results were shown in Table 3. The EIS results agreed with the potentiodynamic polarization findings.

Fig. 3D and E shows the H_2 evolution and variation in pH values. As expected, 0.6Sr showed the fastest release of H_2 and maximum pH change, followed by 0.4Sr, 0Sr, and 0.2Sr. The pH changed sharply during the initial stage and stabilized after 40 h of immersion. The

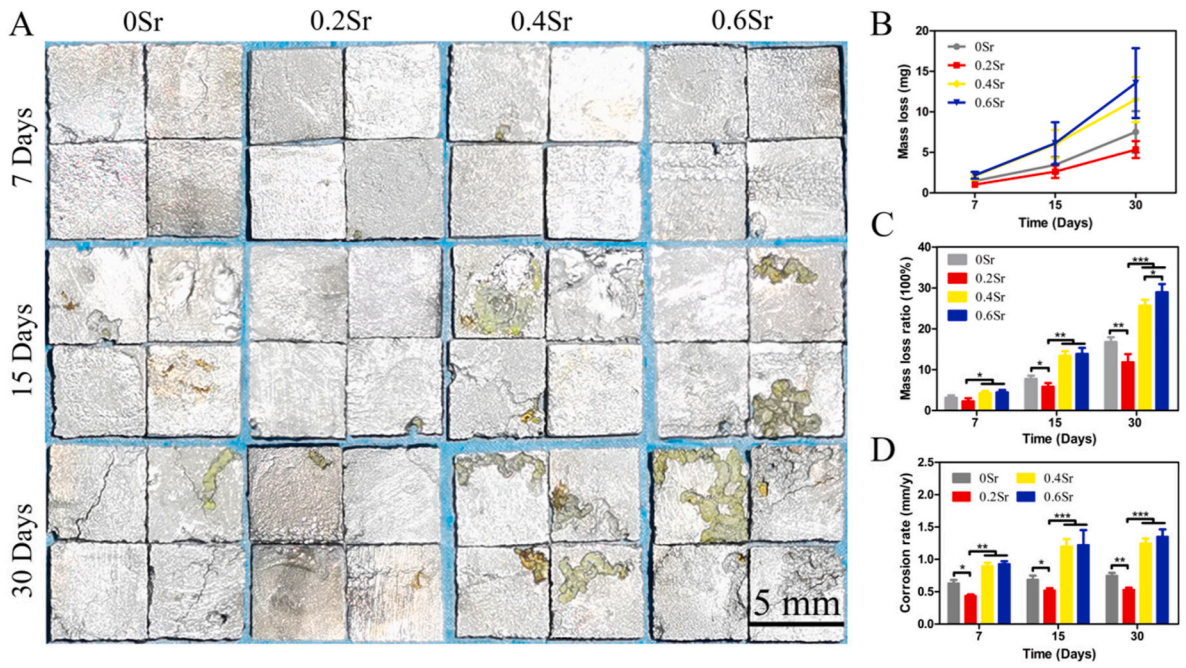

Fig. 10. (A) Corrosion topographies, (B) mass loss, (C) mass loss ratio and (D) corrosion rate of the Mg–1Zn–1Sn-xSr alloys after subcutaneous implantation for 7, 15, and 30 days. Values are the mean ± SD, n = 4. *p < 0.05, **p < 0.01 and ***p < 0.001.

amount of H_2 released accumulates over time, and the H_2 evolution rate of 0.6Sr, 0.4Sr and 0Sr increased, while that for 0.2Sr remained relatively low (the H_2 evolution rate on day 7 was as low as 0.08 ml/cm^2/d). Fig. 3F shows the result of the corrosion rate calculated according to the weight loss, and 0.2Sr had the best corrosion resistance (0.55 ± 0.08 mm/y); the order of the corrosion rate was 0.6Sr > 0.4Sr > 0Sr > 0.2Sr.

Fig. 4A shows the surface topographies and elemental compositions of the Mg–1Zn–1Sn-xSr alloys and p-Mg, as well as the topographies on the cross section observed by SEM. The corrosion product on the surface of the p-Mg had an uneven thickness and was in the form of crystal clusters. The corrosion product layer on the surface of the Mg–1Zn–1Sn-xSr alloys was uniform and dense with deposited white clusters/particles, and the corrosion products gradually increased with increasing Sr content. On the cross section, p-Mg showed typical characteristics of pitting corrosion. The Mg–1Zn–1Sn-xSr samples exhibited a uniform corrosion layer, which was considered to be the result of a change in the corrosion mechanism. Despite similar local corrosion topographies, 0.2Sr had much shallower corrosion beneath the surface. The visible cracks and holes in the corrosion products of the 0.4Sr and 0.6Sr alloys indicated the possibility for penetration of Cl^- and other ions. The EDS results of the corrosion products mainly demonstrated the presence of oxygen, magnesium, phosphorous and calcium, as shown in Fig. 4A and B. The XRD patterns shown in Fig. 4C revealed that the corrosion products of the Mg–Zn–Sn-xSr alloys were mainly composed of Mg $(OH)_2$. With increasing Sr content, the diffraction peak intensity of the corrosion products gradually increased, indicating that the alloy degraded faster during the immersion process. Moreover, the XPS results confirmed the existence of SnO/SnO_2 on the surface of the 0Sr and 0.2Sr samples after immersion in HBSS for 3 h, both of which were reported to not only take part in protective film formation but also improve the corrosion resistance of the substrate [37]. However, the SnO/SnO_2 peaks were significantly weaker on the 0.4Sr and 0.6Sr samples (Fig. S3).

3.3. In vitro cytotoxicity and viability evaluations

The viability of MC3T3-E1 cells cultured in extracts is shown in Fig. 5E. All Sr-containing Mg–1Zn–1Sn-based alloys exhibited good cytocompatibility and even promoted cell proliferation. Among them, the 0.2Sr alloy had the strongest ability to promote cell proliferation, which may be related to its best corrosion resistance. According to ISO 10993-5, the cytotoxicity of Mg–1Zn–1Sn-xSr alloys should be Grade 0 or Grade 1. The cell apoptosis and cycle results are shown in Fig. 5A,B and 5(C,D). Compared with that of the control group, the proportion of S-phase cells in the p-Mg and Mg–1Zn–1Sn-xSr alloys increased, and the proportion of S-phase cells of 0.2Sr reached 27.30%, which is significantly higher than that of the control group (19.50%). This indicates that the Mg–1Zn–1Sn-0.2Sr alloy had a proliferation-promoting effect on cells. Simultaneously, the apoptosis test also confirmed that the Mg–1Zn–1Sn-xSr alloys did not cause cell apoptosis.

Fig. 6 shows the live/dead staining images of MCET3-E1 cells cocultured with extracts for 24, 48 and 72 h. At 24 h, live cells were noticed in all groups, and few dead cells were also found. With the extension of the culture time, the number of cells gradually increased. When time extended to 72 h, a large number of live cells in all Mg–1Zn–1Sn-xSr groups almost filled the entire field of view, while dead cells were hard to find. The live/dead cell assay results confirmed the excellent cytocompatibility of the Mg–1Zn–1Sn-xSr alloys.

3.4. MC3T3-E1 cells in direct culture with Mg–1Zn–1Sn-xSr alloys

Fluorescence images from the 24, 48, and 72 h direct cultures on the surfaces of the Mg–1Zn–1Sn-xSr alloys, p-Mg, and glass reference are shown in Fig. 7A, and the quantitatively analyzed cell adhesion density and F-actin area are shown in Fig. 7B and C, respectively. Attached cells were observed on all substrates studied throughout the 72 h period. The cell adhesion densities on 0Sr, 0.2Sr, 0.4Sr and 0.6Sr were comparable to the glass reference during the first 24 h, while that for p-Mg was significantly lower. At 48 and 72 h, the 0.2Sr group had a significantly higher cell adhesion density than the other groups.

The ion concentrations of the Mg–1Zn–1Sn-xSr alloys, p-Mg, glass reference and DMEM blank control for all incubation time points are summarized in Fig. 7D. At 24, 48 and 72 h, there were higher Mg ion concentrations in the media of the p-Mg and Mg–1Zn–1Sn-xSr alloys compared with those of the glass reference and DMEM blank control. The Mg ion concentration from high to low was ranked as p-Mg>0.6Sr

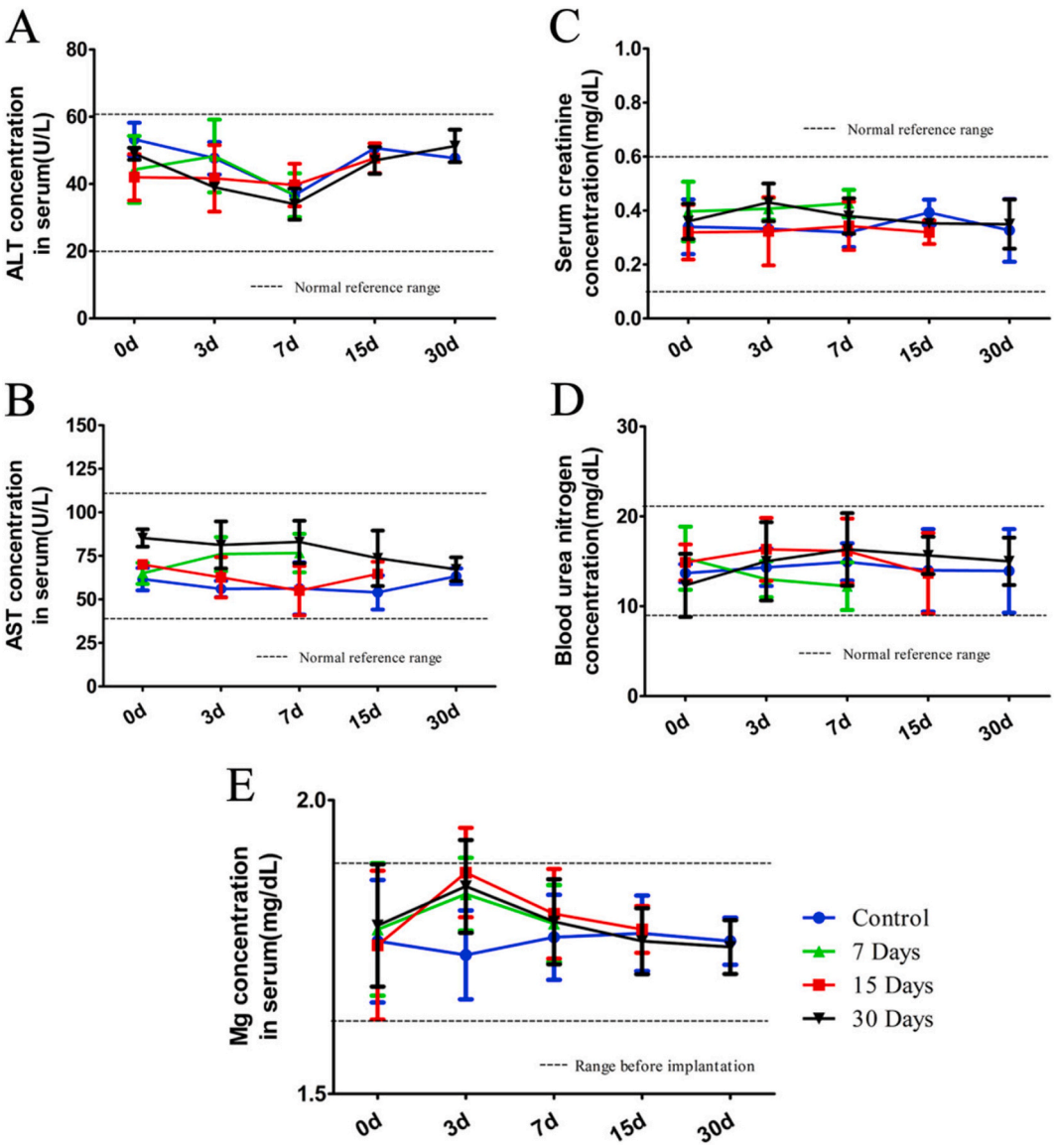

Fig. 11. Levels of the main serum biochemical indicators of liver and kidney function before and after implantation. (A) ALT, (B) AST, (C) CREA, (D) BUN and (E) serum magnesium.

> 0.4Sr > 0Sr > 0.2Sr. In addition, significantly higher Zn and Sn ion concentrations were observed in the media of the 0Sr, 0.2Sr, 0.4Sr, and 0.6Sr samples than those for the glass reference, DMEM blank control and p-Mg at all time points. However, compared with those for 0Sr, 0.4Sr and 0.6Sr, the concentrations of Zn and Sn ions in 0.2Sr were always relatively low. Moreover, the Sr ion concentrations in the media of 0.2Sr, 0.4Sr and 0.6Sr were higher than those in the glass reference, DMEM blank control, p-Mg and 0Sr, which was proportional to the weight percentage of Sr in the alloy.

The pH values of the collected media at 24, 48, and 72 h are summarized in Fig. 7E. The p-Mg (8.11 ± 0.66) and 0.6Sr (8.10 ± 0.08) had the most dramatic pH changes during the first 24 h, and 0Sr (8.06 ± 0.04), 0.2Sr (8.03 ± 0.04), and 0.4Sr (8.04 ± 0.03) had relatively mild changes compared with those of the glass reference (7.92 ± 0.02) and DMEM blank control (7.95 ± 0.03). The overall trend of the pH value of each group at 48 and 72 h was consistent with that at 24 h. The pH for the glass reference media at all incubation intervals was slightly more acidic than that for the DMEM blank control due to cell metabolism.

The surface topographies of Mg–1Zn–1Sn-xSr alloys (x = 0, 0.2, 0.4, and 0.6 wt %) and p-Mg before contact with the media was observed by SEM, as shown in Fig. 8A. Obvious scratches and a small amount of particle-like debris were seen on the surfaces of all samples, which were induced by the polishing of SiC abrasive paper. The cell-substrate interactions were also closely inspected via SEM (Fig. 8B). The cells on p-Mg showed a round shape with limited spreading, strand-like cells were detected on 0Sr samples, while slightly more cord-like cells with few pseudopods were detected on 0.2Sr, 0.4Sr and 0.6Sr samples. Notably, cells on 0.2Sr and 0.4Sr displayed much larger areas and better morphology than the other groups. Interestingly, a network structure layer with micro/nanotopography was formed on the surface of the 0.2Sr, 0.4Sr and 0.6Sr samples which may have great contribution to the adhesion and spreading of cells, but no similar structure was observed on the p-Mg and 0Sr samples.

Mg–1Zn–1Sn-xSr alloys were immersed in HBSS solution or cocultured with MC3T3-E1 cells to determine their H_2 evolution speed. We found that the 0.2Sr alloy results the least H_2 production after 48 h of immersion (Fig. 9). The H_2 evolution changed rapidly during the first hour, and then slowed down. After 3 h of immersion, the H_2 evolution rate decreased significantly, especially for the 0Sr and 0.2Sr samples (Fig. S4 and Supplemental Video 1). The 0.2Sr has the least amount of H_2

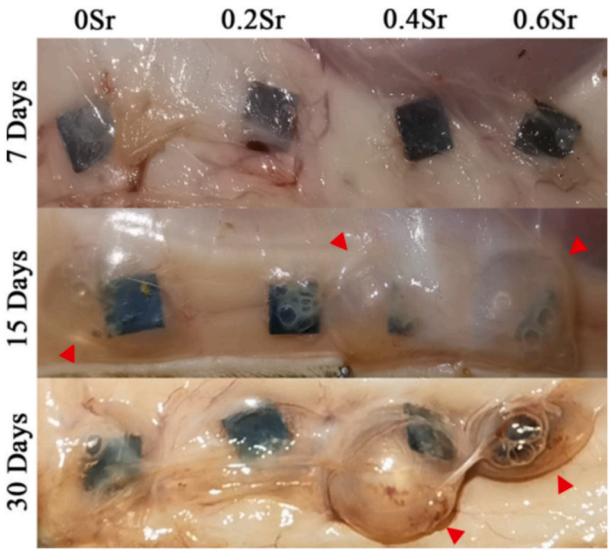

Fig. 12. General observation of Mg–1Zn–1Sn-xSr alloys after subcutaneous implantation for 7, 15, and 30 days. Red triangles indicate H_2 bubbles.

evolution. This result confirmed that adding a proper amount of Sr to the Mg–1Zn–1Sn system can further reduce the release of H_2.

3.5. *In vivo evaluation*

The in vivo anti-corrosion properties of the Mg–1Zn–1Sn-xSr alloys were determined by subcutaneous implantation. Fig. 10A shows the topographies of 0Sr, 0.2Sr, 0.4Sr and 0.6Sr samples after subcutaneous implantation. The degradation increased over time in all samples. Compared to that for 0.4Sr and 0.6Sr, the corrosion of 0Sr and 0.2Sr was slightly milder at 7 and 15 days. After 7 days of implantation, corrosion marks could be seen on the surface of the 0Sr and 0.2Sr samples, while more obvious corrosion pits were formed at the edges of the 0.4Sr and 0.6Sr samples. After 15 and 30 days of implantation, the area of corrosion pits further expanded on the surface of the 0.4Sr and 0.6Sr samples, obvious cracks appeared on the surface of 0Sr. No severe corrosion signs were observed on the 0.2Sr sample indicating its excellent corrosion resistance in vivo. Fig. 10B, C and D shows the mass loss, mass loss ratio and corrosion rate. In the first 7 days, the corrosion rates of Mg–1Zn–1Sn-xSr calculated by mass loss were 0.63 ± 0.05, 0.44 ± 0.02, 0.89 ± 0.05 and 0.93 ± 0.04 mm/y, which were very close to the corrosion rates estimated by HBSS immersion. With prolonged time, the mass loss of 0.4Sr and 0.6Sr was significantly increased, while the 0.2Sr remained at obviously lower levels than those of 0Sr, 0.4Sr and 0.6Sr. At 30 days, the corrosion rates of the Mg–1Zn–1Sn-xSr alloy reached 0.75 ± 0.04, 0.53 ± 0.03, 1.25 ± 0.07 and 1.35 ± 0.11 mm/y, respectively. The corrosion rate of 0.2Sr is still at a relatively low level.

The degradation products from the Mg–1Zn–1Sn-xSr alloys were inevitably released and entered the bloodstream. Therefore, the serum biochemical indices closely related to liver and kidney function and serum magnesium concentration were monitored, and the results are shown in Fig. 11. All SD rats had liver and kidney function indicators within the normal reference range at all observation time points. Additionally, the serum magnesium concentration increased slightly on the 3rd day after implantation, but quickly returned to normal at day 7. These results reveal that the metal ions or particles produced by degradation did not affect liver and kidney function, and the biological safety of Mg–1Zn–1Sn-xSr alloys is reliable.

The general observations of the subcutaneous tissues around the implanted samples are shown in Fig. 12. All implants degraded in vivo and produced H_2, which accumulated within the subcutaneous tissue and formed bubbles. According to the sizes of bubbles, 0.2Sr produced the least amount of H_2 at all time points. H&E staining of subcutaneous tissue is shown in Fig. 13. At the early stage of implantation, all samples caused local tissue inflammation, which gradually eased over time. The subcutaneous tissue attached to the 0.4Sr samples showed a thick fibrous layer, and the 0.6Sr samples sometimes showed more inflammatory cell infiltration in the fibrous layer. The 0.2Sr group presented milder inflammatory reactions and a thinner fibrous layer than the other three groups, suggesting that the 0.2Sr group possessed the best histocompatibility in vivo.

The histological response of organs is the gold standard for evaluating the systemic influence of biodegradable biomaterials during their metabolism and excretion in vivo. The H&E staining of vital organs is shown in Fig. 14. After 7, 15 and 30 days of implantation, no obvious pathological changes occurred in important organ tissues.

4. Discussion

The present study was designed to investigate the influence of the incorporation of a minor amount of Sr into the Mg–1Zn–1Sn-based system. As confirmed by our systemic analysis, by incorporating 0.2 wt % of Sr into the system, the in vitro/vivo corrosion resistance was significantly improved. Simultaneously, the mechanical properties, H_2 evolution, cytocompatibility and histocompatibility were also greatly optimized.

4.1. *Microstructure, mechanical properties and corrosion behavior*

The as-cast Mg–1Zn–1Sr-xSr alloys exhibited a typical dendrite structure that is characteristic of divorced eutectics. The average grain size decreased with Sr addition up to 0.6 wt %, which is consistent with a previous study [19]. The reasons can be ascribed to the following two aspects. First, the addition of a minor amount of Sr increases the supercooling degree in front of the solid-liquid interface, which can increase the crystal nuclei of the primary α-Mg phase. Second, the solid solubility of Sr in Mg is 0.11 wt %, with the Sr addition higher than 0.11 wt%, the redundant Sr would be enriched at the solid/liquid interface and thus form the Sr adsorbed film, which may damage the surface of crystal grains or change the direction of crystal grain growth and inhibit the growth of grains. Therefore, the grain growth slows down and the grains are refined. Interestingly, the average grain size of all as-extruded Mg–1Zn–1Sr-xSr alloys was approximately 20 μm, and the gradual increase in Sr content did not have a significant refinement effect on the as-extruded alloys, this may be due to the obvious coarsening of the alloy structure after the homogenization heat treatment, and the final refined grains were attributed to the refinement of the structure by hot extrusion. Different sizes and dot-like crystal grain second phases existed in the alloy and had a nonuniform microstructure, which may be caused by incomplete dynamic recrystallization during hot extrusion [38,39]. In this study, most of the added Zn and Sn dissolved into the alloy matrix due to their low content and high solid solubility in Mg, and the second phase was difficult to detect with XRD. Only a small amount of $Mg_{17}Sr_2$ and MgZn phases were detected in 0.6Sr alloy, which was consistent with previous studies [15,40–43].

The improved strength was mainly derived from the second phase strengthening and the morphology of the eutectic structures. Due to the low solid solubility of Sr in Mg, the second phase containing Sr readily precipitated at the grain boundaries during solidification, and the net-like second phases acted as a skeleton during the transmission and distribution of stresses. After hot extrusion, the broken second-phase particles were evenly distributed in the matrix, as shown in Fig. 1. During plastic deformation, the second-phase particles pinned dislocations, which obstructed the movement of the dislocations, thereby improving the mechanical strength by providing dispersion strengthening [44,45]. Additionally, the solution strengthening effect can also be caused by the minor amount of Sr [34]. However, the superabundance of Sr to form more $Mg_{17}Sr_2$ secondary phases significantly deteriorated the plasticity

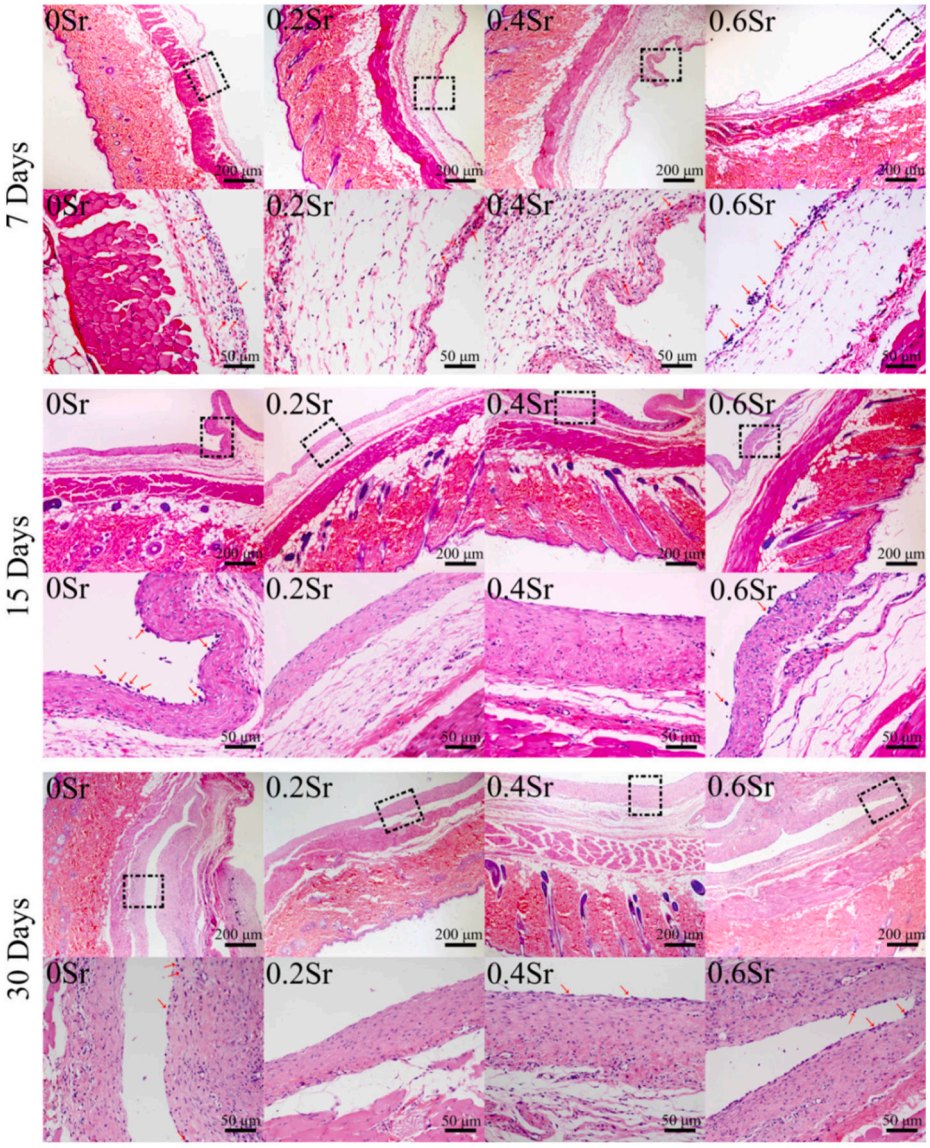

Fig. 13. Photomicrographs of subcutaneous tissue sections of Mg–1Zn–1Sn-xSr alloys after subcutaneous implantation for 7, 15 and 30 days. The scale bar = 200 μm. The dotted boxes were taken at 200 times the original magnification with a scale bar = 50 μm. The red arrow indicates leukocytes.

of the alloy. The mechanical properties obtained in this study match well with human bone tissue.

From the perspective of material characterization, grain refinement is an important factor that has been shown to contribute to the improvement of corrosion resistance. On the one hand, the Sr addition brings about the grain refinement of the Mg–1Zn–1Sn alloy. On the other hand, the Sr addition leads to the higher volume fraction of intermetallics, which leads to the micro galvanic coupling and is detrimental to corrosion resistance. When the corrosion-blocking effect of the second phase at the grain boundary is less than the accelerated corrosion effect associated with the micro-galvanic cells, the corrosion resistance of the alloy will be reduced. Therefore, the 0.4Sr and 0.6Sr alloys exhibit the inferior corrosion resistance to the 0.2Sr alloy.

From an electrochemical point of view, it was easy to form a relatively complete protective film on the alloy surface when the E_{corr} was low; however, the protective film was destroyed, and the anode i_{corr} increased significantly when the E_{corr} reached the breakdown value. Adding a proper amount of Sr ($\leq$0.2 wt %) can increase the E_{corr} of the matrix and decrease the i_{corr} to enhance the corrosion resistance. However, an excessive amount of Sr results in the formation of additional high-potential second phases, which increases the probability of galvanic corrosion and deteriorates the corrosion resistance. This may be the reason why there was no breakdown potential in 0.6Sr.

Sn also plays an important role in enhancing the corrosion resistance of the alloy. According to the Pourbaix E-pH diagram of Sn–H_2O [45], SnH_4 might form first, which was reported to react with water to form SnO_2(Eq. (1)) [46].

$$SnH_4 + 2H_2O \rightarrow SnO_2 + 3H_2 \quad (1)$$

The protective layer composed of $Mg(OH)_2$ and Sn oxide (SnO/SnO_2) was more efficient barrier against corrosion than $Mg(OH)_2$ [47], and the greater amount of SnO_2 integrated in the surface offers stronger protection against corrosion [48]. This illustrates well the reason why 0Sr and 0.2Sr alloys possess better corrosion performance than 0.4Sr and 0.6Sr. In addition, Sn had a higher H_2 overpotential than the Mg matrix [37,49]. When the matrix corroded, the metallic Sn was spontaneously enriched on the surface of the matrix to act as a cathode, which can effectively capture the H atom than the matrix and inhibit the H_2 evolution rate [50]. It has been pointed out that controlling the H_2 evolution rate is also an effective solution to improve the corrosion resistance of Mg-based alloys [51,52].

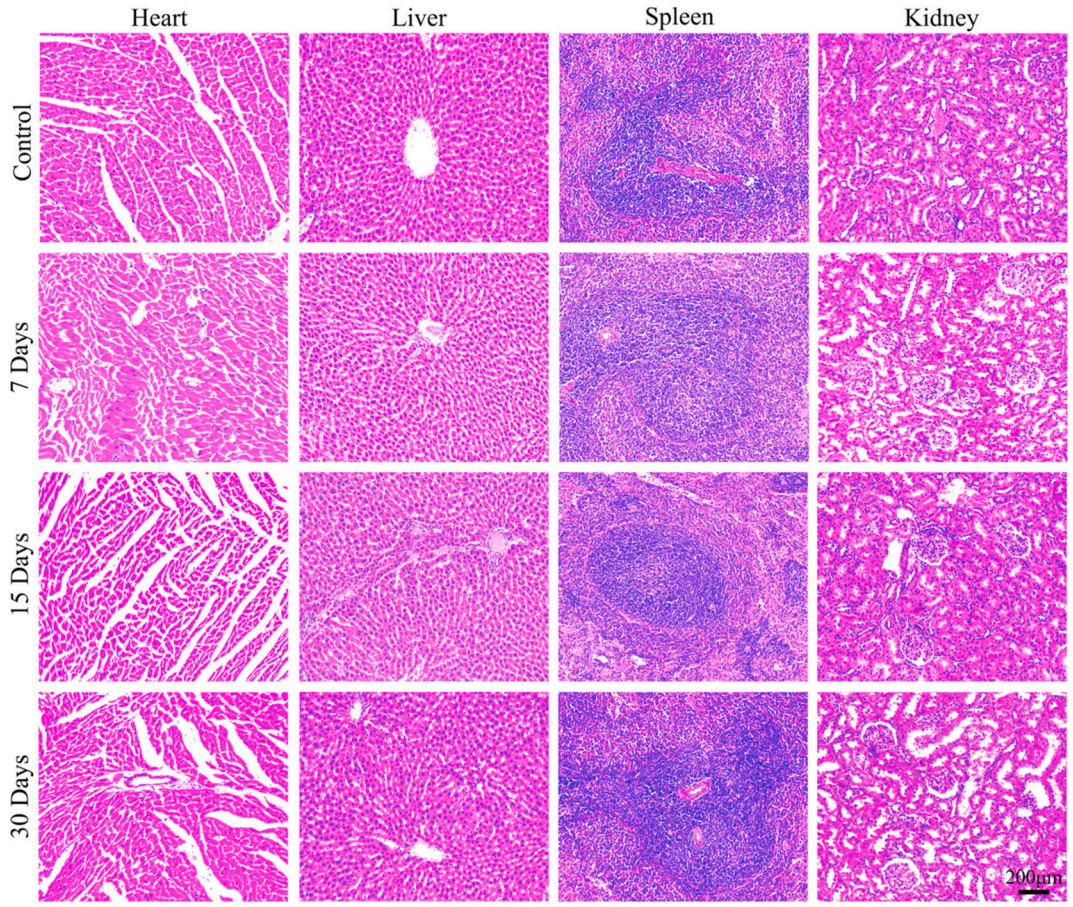

Fig. 14. H&E staining of heart, liver, spleen and kidney organs after implantation of Mg–1Zn–1Sn-xSr alloys for 7, 15 and 30 day. The scale bar = 200 μm.

4.2. In vitro cytocompatibility evolution

Regarding the selection of alloying elements, biological safety is the primary consideration, and corrosion products need to be nontoxic and able to be absorbed by surrounding tissues or excreted via the kidney. Our in vitro studies demonstrated that Mg–1Zn–1Sn-xSr alloys had excellent cytocompatibility. In particular, the cell viability was significantly increased due to the incorporation of Sr, which is consistent with previous studies [22,34,53]. Cell adhesion on the surface of the material is a prerequisite for cell growth, migration and differentiation [54]. In the present study, MC3T3-E1 cells had satisfactory adhesion and proliferation on the surfaces of Mg–1Zn–1Sn-xSr, as shown in Figs. 7 and 8. This may be attributed to the following reasons. First, all alloying elements selected are essential nutrients for the human body, and the solubilized Mg, Zn, Sn and Sr ions in the medium were far below the therapeutic daily dosages reported in the literature [55,56]. Second, the solid-dissolved Sn element in the Mg-matrix had a significant inhibitory effect on the H_2 evolution, which reduced the interference of H_2 evolution on cell adhesion and proliferation [18,57]. Simultaneously, a protective layer composed of $Mg(OH)_2$ and Sn oxide (SnO/SnO_2) could be formed on the sample surface in a short time (Figure S5A,B and C), which results in a greater enhancement of corrosion performance [47]. Moreover, the incorporation of Sr not only improved the corrosion resistance but also increased the proliferation of preosteogenic cells [57].

In particular, a network structure layer with micro/nanotopography can spontaneously formed on the surface of 0.2Sr, 0.4Sr and 0.6Sr after 1 h of immersion in DMEM medium, and gradually takes shape within 6 h (Fig. S5D). The aforementioned phenomena was also observed in HBSS solution (Fig. S5E). However, no similar structure was observed on the 0Sr sample. These results suggested that the Sr microalloyed into the Mg–1Zn–1Sn system may play a crucial role in the formation of this layer. Coincidentally, Geng et al. [58] fabricated Sr-containing coatings with a sheet-like or needle-like structure via electrochemical deposition on the surface of titanium-based alloys, which is similar to our findings. In summary, Sn ions inhibiting H_2 evolution , Sr ions enhancing cell viability and the network structure layer spontaneously formed on the surface of materials may play key roles in promoting cell adhesion, proliferation and spreading.

4.3. In vivo corrosion resistance and histocompatibility

The in vivo corrosive environment is different from the in vitro environment [59,60]. A subcutaneous implantation animal model was used to further verify the corrosion resistance and histocompatibility of the Mg–1Zn–1Sn-xSr alloys. As shown in Fig. 10, all samples underwent different degrees of degradation over time. Seven days after implantation, there was no significant difference in the degree of corrosion and mass loss in each group. This may be because Mg–1Zn–1Sn-xSr alloys themselves have excellent corrosion resistance and the protective effect of the mixed $Mg(OH)_2$ and Sn oxide (SnO/SnO_2) layer. With an extension of the time, the protective film was gradually destroyed, and corrosion differences between Mg–1Zn–1Sn-xSr alloys gradually appeared. When the Sr content was 0.2 wt %, the corrosion-blocking effect of the second phase at the grain boundaries was greater than the accelerated corrosion effect associated with the microgalvanic cells [61]. This relationship was destroyed when the Sr content exceeded 0.2 wt %, the reaction of the microgalvanic cell increased and the corrosion resistance deteriorated. The degradation rate in vivo was on the order of 0.2Sr < 0Sr < 0.4Sr < 0.6Sr, which was consistent with the results in

vitro.

Although studies have reported that the degradation rate of Mg–Zn-based alloys in vivo is relatively fast [62,63], and the resulting H_2 accumulation affects surrounding tissues when used as orthopedic implants [42] or influences the effectiveness of implants by precipitating at the implant-tissue interface [64]. However, in the present study, we were surprised to find that there was no obvious H_2 cavity formation around the 0.2Sr samples at all observation time points, only a few bubbles were seen at 15 days. It was reported that the adsorption of H_2 from subcutaneous gas pockets in rats was limited by the diffusion coefficient of H_2 in the tissue [65]. Song [66] reported that a H_2 release rate of 0.01 mL cm^2 per day can be tolerated by the body without causing damage. Thus, we infer that the H_2 evolution rate of 0.2Sr in vivo approaches or reaches 0.01 mL cm^2 per day. Witte et al. [67] demonstrated significantly higher corrosion rates at the subcutaneous implantation site than the corrosion rate in bone. Therefore, we speculate that the amount of H_2 evolution of 0.2Sr in the bone will be further reduced, which is worthy of further study.

The blood biochemical results showed that there are no obvious abnormalities in ALT, AST, CREA, BUN and Mg ions, Furthermore, histological examination also confirmed that no significant metal ion deposition (Fig. S6) or obvious pathological changes occurred in vital organs. The H&E staining results of subcutaneous tissue showed that the 0.2Sr possessed the best histocompatibility in vivo, which may have resulted from the minimal corrosive products and no obvious effect on the chemical balance in the local biological environment [68]. Although the inflammatory response in other groups was slightly more severe than in the 0.2Sr group, there was no significant difference compared with the inflammatory response of Ti–6Al–4V subcutaneous implantation reported by L. Elkaiam et al. [69]. These results demonstrated that Mg–1Zn–1Sn-xSr alloys had excellent biocompatibility in vivo.

5. Conclusion

In this study, to explore the feasibility of Mg–1Zn–1Sn-xSr (x = 0, 0.2, 0.4, and 0.6 wt%) alloys as biodegradable materials, their corrosion, mechanical properties, H_2 evolution and biocompatibility in vitro/vivo were systematically investigated. The main findings are as follows:

1. A minor amount of Sr (≤0.2 wt %) enhanced the corrosion resistance of Mg–1Zn–1Sn-based alloy through grain refinement, increasing corrosion potential and decreasing corrosion current density, while an excessive amount of Sr (>0.2 wt %) deteriorated the corrosion resistance. The mechanical strength gradually increased with increasing Sr content, which is comparable to those of natural cortical bone.
2. In vitro experiments demonstrated that Mg–1Zn–1Sn-0.2Sr has extremely low H_2 evolution rate, excellent cytocompatibility and biological activity. More importantly, we discovered and reported for the first time that Sr-containing Mg–1Zn–1Sn-based alloys had the ability to spontaneously form a network structure layer with micro/nanotopography, which was conducive to cell proliferation, adhesion and spreading.
3. In vivo assessments confirmed that all Mg–1Zn–1Sn-xSr alloys exhibited excellent biosafety and good histocompatibility. Preliminary results indicated that the Mg–1Zn–1Sn-0.2Sr alloy had the best corrosion resistance (0.53 mm/y) and the least H_2 evolution. This alloy stood out as a promising candidate to be further studied for orthopedic implant applications.

CRediT authorship contribution statement

Yafeng Wen: Methodology, Investigation, Formal analysis, Writing – original draft. **Qingshan Liu:** Formal analysis, Writing – original draft. **Jingfeng Wang:** Supervision. **Qiming Yang:** Formal analysis. **Weikang Zhao:** Formal analysis. **Bo Qiao:** Supervision. **Yuling Li:** Formal analysis. **Dianming Jiang:** Supervision, Conceptualization, Writing – review & editing.

Declaration of competing interest

None.

Acknowledgements

The authors are grateful for the financial support from the the National Natural Science Foundation of China (51874062); the Chongqing foundation and advanced research project (cstc2019jcyj-zdxmX0010); Project No. 2018CDGFCL0005 and No. 2019CDXYCL0031 supported by the Fundamental Research Funds for the Central Universities and the Basic Research and Frontier Exploration General Project of Chongqing Science and Technology Commission (no:cstc2018jcyjA0543). Foundation for Young Scientist of the Medical Association of Sichuan Province (Q19069); The Research Foundation of science and technology bureau of Nanchong City (18SXHZ0147).

Appendix A. Supplementary data

Supplementary data to this article can be found online at https://doi.org/10.1016/j.bioactmat.2021.04.043.

References

[1] Y. Zhang, J. Xu, Y.C. Ruan, M.K. Yu, M. O'Laughlin, H. Wise, D. Chen, L. Tian, D. Shi, J. Wang, S. Chen, J.Q. Feng, D.H. Chow, X. Xie, L. Zheng, L. Huang, S. Huang, K. Leung, N. Lu, L. Zhao, H. Li, D. Zhao, X. Guo, K. Chan, F. Witte, H. C. Chan, Y. Zheng, L. Qin, Implant-derived magnesium induces local neuronal production of CGRP to improve bone-fracture healing in rats, Nat. Med. 22 (10) (2016) 1160–1169.

[2] Y. Li, S. Zhao, S. Li, Y. Ge, R. Wang, L. Zheng, J. Xu, M. Sun, Q. Jiang, Y. Zhang, H. Wei, Surface engineering of biodegradable magnesium alloys for enhanced orthopedic implants, Small 15 (51) (2019), e1904486.

[3] K. Munir, J. Lin, C. Wen, P.F.A. Wright, Y. Li, Mechanical, corrosion, and biocompatibility properties of Mg-Zr-Sr-Sc alloys for biodegradable implant applications, Acta Biomater. 102 (2020) 493–507.

[4] J. Wang, Y. Wu, H. Li, Y. Liu, X. Bai, W. Chau, Y. Zheng, L. Qin, Magnesium alloy based interference screw developed for ACL reconstruction attenuates peri-tunnel bone loss in rabbits, Biomaterials 157 (2018) 86–97.

[5] Y. Chen, Z. Xu, C. Smith, J. Sankar, Recent advances on the development of magnesium alloys for biodegradable implants, Acta Biomater. 10 (11) (2014) 4561–4573.

[6] M.P. Staiger, A.M. Pietak, J. Huadmai, G. Dias, Magnesium and its alloys as orthopedic biomaterials: a review, Biomaterials 27 (9) (2006) 1728–1734.

[7] F. Witte, The history of biodegradable magnesium implants: a review, Acta Biomater. 6 (5) (2010) 1680–1692.

[8] H. Windhagen, K. Radtke, A. Weizbauer, J. Diekmann, Y. Noll, U. Kreimeyer, R. Schavan, C. Stukenborg-Colsman, H. Waizy, Biodegradable magnesium-based screw clinically equivalent to titanium screw in hallux valgus surgery: short term results of the first prospective, randomized, controlled clinical pilot study, Biomed. Eng. Online 12 (2013) 62.

[9] M. Haude, H. Ince, A. Abizaid, R. Toelg, P.A. Lemos, C. von Birgelen, E. H. Christiansen, W. Wijns, F.-J. Neumann, C. Kaiser, E. Eeckhout, S.T. Lim, J. Escaned, H.M. Garcia-Garcia, R. Waksman, Safety and performance of the second-generation drug-eluting absorbable metal scaffold in patients with de-novo coronary artery lesions (BIOSOLVE-II): 6 month results of a prospective, multicentre, non-randomised, first-in-man trial, Lancet 387 (2016) 31–39, 10013.

[10] F. Witte, J. Fischer, J. Nellesen, H.A. Crostack, V. Kaese, A. Pisch, F. Beckmann, H. Windhagen, In vitro and in vivo corrosion measurements of magnesium alloys, Biomaterials 27 (7) (2006) 1013–1018.

[11] W. Ding, Opportunities and challenges for the biodegradable magnesium alloys as next-generation biomaterials, Regenerative Biomaterials 3 (2) (2016) 79–86.

[12] F. Witte, V. Kaese, H. Haferkamp, E. Switzer, A. Meyer-Lindenberg, C.J. Wirth, H. Windhagen, In vivo corrosion of four magnesium alloys and the associated bone response, Biomaterials 26 (17) (2005) 3557–3563.

[13] X. Gu, Y. Zheng, Y. Cheng, S. Zhong, T. Xi, In vitro corrosion and biocompatibility of binary magnesium alloys, Biomaterials 30 (4) (2009) 484–498.

[14] M. Salahshoor, Y. Guo, Biodegradable orthopedic magnesium-calcium (MgCa) alloys, processing, and corrosion performance, Materials 5 (1) (2012) 135–155.

[15] M. Bornapour, N. Muja, D. Shum-Tim, M. Cerruti, M. Pekguleryuz, Biocompatibility and biodegradability of Mg-Sr alloys: the formation of Sr-substituted hydroxyapatite, Acta Biomater. 9 (2) (2013) 5319–5330.

[16] E. Zhang, L. Yang, J. Xu, H. Chen, Microstructure, mechanical properties and biocorrosion properties of Mg–Si(–Ca, Zn) alloy for biomedical application, Acta Biomater. 6 (5) (2010) 1756–1762.

[17] C. Shuai, Y. Zhou, X. Lin, Y. Yang, C. Gao, X. Shuai, H. Wu, X. Liu, P. Wu, P. Feng, Preparation and characterization of laser-melted Mg-Sn-Zn alloys for biomedical application, J. Mater. Sci. Mater. Med. 28 (1) (2017) 13.

[18] W. Jiang, J. Wang, Q. Liu, W. Zhao, D. Jiang, S. Guo, Low hydrogen release behavior and antibacterial property of Mg-4Zn-xSn alloys, Mater. Lett. 241 (2019) 88–91.

[19] M. Cheng, J. Chen, H. Yan, B. Su, Z. Yu, W. Xia, X. Gong, Effects of minor Sr addition on microstructure, mechanical and bio-corrosion properties of the Mg-5Zn based alloy system, J. Alloys Compd. 691 (2017) 95–102.

[20] H.S. Brar, J. Wong, M.V. Manuel, Investigation of the mechanical and degradation properties of Mg–Sr and Mg–Zn–Sr alloys for use as potential biodegradable implant materials, J Mech Behav Biomed Mater 7 (2012) 87–95.

[21] M. Pilmane, K. Salma-Ancane, D. Loca, J. Locs, L. Berzina-Cimdina, How strontium ranelate, via opposite effects on bone resorption and formation, prevents osteoporosis, Mater. Sci. Eng. C 78 (2017) 1222–1230.

[22] P.J. Marie, D. Felsenberg, M.L. Brandi, How strontium ranelate, via opposite effects on bone resorption and formation, prevents osteoporosis, Osteoporos. Int. 22 (2010) 1659–1667.

[23] A.F. Cipriano, A. Sallee, R.-G. Guan, A. Lin, H. Liu, A comparison study on the degradation and cytocompatibility of Mg-4Zn-xSr alloys in direct culture, ACS Biomater. Sci. Eng. 3 (2017) 540–550.

[24] Z. Gao, M. Song, R.L. Liu, Y. Shen, L. Ward, I. Cole, X.B. Chen, X. Liu, Improving in vitro and in vivo antibacterial functionality of Mg alloys through micro-alloying with Sr and Ga, Mater Sci Eng C Mater Biol Appl 104 (2019), 109926.

[25] B.-J. Lv, S. Wang, T.-W. Xu, F. Guo, Effects of minor Nd and Er additions on the precipitation evolution and dynamic recrystallization behavior of Mg–6.0Zn–0.5Mn alloy, J. Magnes. Alloys (2020), https://doi.org/10.1016/j.jma.2020.06.018.

[26] A. Gungor, A. Incesu, Effects of alloying elements and thermomechanical process on the mechanical and corrosion properties of biodegradable Mg alloys, J. Magnes. Alloys (2020), https://doi.org/10.1016/j.jma.2020.09.009.

[27] A.F. Cipriano, A. Sallee, M. Tayoba, M.C. Cortez Alcaraz, A. Lin, R.G. Guan, Z. Y. Zhao, H. Liu, Cytocompatibility and early inflammatory response of human endothelial cells in direct culture with Mg-Zn-Sr alloys, Acta Biomater. 48 (2017) 499–520.

[28] ASTM-G31-72, Standard Practice for Laboratory Immersion Corrosion Testing of Metals, Annual Book of ASTM Standards, American Society for Testing and Materials, Philadelphia, Pennsylvania, USA, 2004.

[29] J. Li, L. Tan, P. Wan, X. Yu, K. Yang, Study on microstructure and properties of extruded Mg–2Nd–0.2Zn alloy as potential biodegradable implant material, Mater Sci Eng C Mater Biol Appl 49 (2015) 422–429.

[30] J. Wang, F. Witte, T. Xi, Y. Zheng, K. Yang, Y. Yang, D. Zhao, J. Meng, Y. Li, W. Li, K. Chan, L. Qin, Recommendation for modifying current cytotoxicity testing standards for biodegradable magnesium-based materials, Acta Biomater. 21 (2015) 237–249.

[31] H. Lai, J. Li, J. Li, Y. Zhang, Y. Xu, Effects of Sr on the microstructure, mechanical properties and corrosion behavior of Mg-2Zn-xSr alloys, J. Mater. Sci. Mater. Med. 29 (2018) 87.

[32] F. Peng, H. Li, D. Wang, P. Tian, Y. Tian, G. Yuan, D. Xu, X. Liu, Enhanced corrosion resistance and biocompatibility of magnesium alloy by Mg−Al-layered double hydroxide, ACS Appl. Mater. Interfaces 8 (2016) 35033–35044.

[33] H. Li, Q. Peng, X. Li, K. Li, Z. Han, D. Fang, Microstructures, mechanical and cytocompatibility of degradable Mg–Zn based orthopedic biomaterials, Mater. Des. 58 (2014) 43–51.

[34] D. Jiang, Y. Dai, Y. Zhang, C. Liu, K. Yu, Effects of Strontium addition on microstructure, mechanical properties, corrosion properties and cytotoxicity of Mg–1Zn–1Mn alloy, Mater. Res. Express 6 (2019).

[35] Z. Li, M. Chen, W. Li, H. Zheng, C. You, D. Liu, F. Jin, The synergistic effect of trace Sr and Zr on the microstructure and properties of a biodegradable Mg-Zn-Zr-Sr alloy, J. Alloys Compd. 702 (2017) 290–302.

[36] ISO 10993-52009(E), Biological Evaluation of Medical Devices—Part 5 Tests for in Vitro Cytotoxicity, International Organization for Standardization, 2009.

[37] X. Liu, D. Shan, Y. Song, R. Chen, E. Han, Influences of the quantity of Mg2Sn phase on the corrosion behavior of Mg–7Sn magnesium alloy, Electrochim. Acta 56 (2011) 2582–2590.

[38] T. Abu Leil, N. Hort, W. Dietzel, C. Blawert, Y. Huang, K.U. Kainer, K.P. Rao, Microstructure and corrosion behavior of Mg-Sn-Ca alloys after extrusion, Trans. Nonferrous Metals Soc. China 19 (2009) 40–44.

[39] X. Zhang, G. Yuan, J. Niu, P. Fu, W. Ding, Microstructure, mechanical properties, biocorrosion behavior, and cytotoxicity of as-extruded Mg–Nd–Zn–Zr alloy with different extrusion ratios, J Mech Behav Biomed Mater 9 (2012) 153–162.

[40] Y. Ding, Y. Li, C. Wen, Effects of Mg17Sr2 phase on the bio-corrosion behavior of Mg–Zr–Sr alloys, Adv. Eng. Mater. 18 (2016) 259–268.

[41] M. Masoumi, M. Pekguleryuz, The influence of Sr on the microstructure and texture evolution of rolled Mg–1%Zn alloy, Mater. Sci. Eng., A 529 (2011) 207–214.

[42] X.N. Gu, X.H. Xie, N. Li, Y.F. Zheng, L. Qin, In vitro and in vivo studies on a Mg–Sr binary alloy system developed as a new kind of biodegradable metal, Acta Biomater. 8 (2012) 2360–2374.

[43] R.G. Guan, A.F. Cipriano, Z.Y. Zhao, J. Lock, D. Tie, T. Zhao, T. Cui, H. Liu, Development and evaluation of a magnesium–zinc–strontium alloy for biomedical applications — alloy processing, microstructure, mechanical properties, and biodegradation, Mater Sci Eng C Mater Biol Appl 33 (2013) 3661–3669.

[44] S. Queyreau, G. Monnet, B. Devincre, Orowan strengthening and forest hardening superposition examined by dislocation dynamics simulations, Acta Mater. 58 (2010) 5586–5595.

[45] P.-W. Chu, E. Le Mire, E.A. Marquis, Microstructure of localized corrosion front on Mg alloys and the relationship with hydrogen evolution, Corrosion Sci. 128 (2017) 253–264.

[46] J. Wang, Y. Li, S. Huang, X. Zhou, Study of the corrosion behavior and the corrosion films formed on the surfaces of Mg–xSn alloys in 3.5 wt.% NaCl solution, Appl. Surf. Sci. 317 (2014) 1143–1150.

[47] J. Kubasek, D. Vojtech, J. Lipov, T. Ruml, Structure, mechanical properties, corrosion behavior and cytotoxicity of biodegradable Mg–X (X=Sn, Ga, In) alloys, Mater Sci Eng C Mater Biol Appl 33 (2013) 2421–2432.

[48] W. Du, K. Liu, K. Ma, Z. Wang, S. Li, Effects of trace Ca/Sn addition on corrosion behaviors of biodegradable Mg–4Zn–0.2Mn alloy, Journal of Magnesium and Alloys 6 (2018) 1–14.

[49] O. Azizi, M. Jafarian, F. Gobal, H. Heli, M.G. Mahjani, The investigation of the kinetics and mechanism of hydrogen evolution reaction on tin, Int. J. Hydrogen Energy 32 (2007) 1755–1761.

[50] H.-Y. Ha, J.-Y. Kang, J. Yang, C.D. Yim, B.S. You, Role of Sn in corrosion and passive behavior of extruded Mg-5 wt%Sn alloy, Corrosion Sci. 102 (2016) 355–362.

[51] H.-Y. Ha, J.-Y. Kang, S.G. Kim, B. Kim, S.S. Park, C.D. Yim, B.S. You, Influences of metallurgical factors on the corrosion behaviour of extruded binary Mg–Sn alloys, Corrosion Sci. 82 (2014) 369–379.

[52] H.-Y. Ha, J.-Y. Kang, C.D. Yim, J. Yang, B.S. You, Role of hydrogen evolution rate in determining the corrosion rate of extruded Mg-5Sn-(1-4 wt%)Zn alloys, Corrosion Sci. 89 (2014) 275–285.

[53] J. Braux, F. Velard, C. Guillaume, S. Bouthors, E. Jallot, J.M. Nedelec, D. Laurent-Maquin, P. Laquerriere, A new insight into the dissociating effect of strontium on bone resorption and formation, Acta Biomater. 7 (2011) 2593–2603.

[54] C. Liang, H. Wang, J. Yang, Y. Cai, X. Hu, Y. Yang, B. Li, H. Li, H. Li, C. Li, X. Yang, Femtosecond laser-induced micropattern and Ca/P deposition on Ti implant surface and its acceleration on early osseointegration, ACS Appl. Mater. Interfaces 5 (2013) 8179–8186.

[55] D. Bian, W. Zhou, J. Deng, Y. Liu, W. Li, X. Chu, P. Xiu, H. Cai, Y. Kou, B. Jiang, Y. Zheng, Development of magnesium-based biodegradable metals with dietary trace element germanium as orthopaedic implant applications, Acta Biomater. 64 (2017) 421–436.

[56] A.F. Cipriano, T. Zhao, I. Johnson, R.G. Guan, S. Garcia, H. Liu, In vitro degradation of four magnesium–zinc–strontium alloys and their cytocompatibility with human embryonic stem cells, J. Mater. Sci. Mater. Med. 24 (2013) 989–1003.

[57] X. Yan, P. Wan, L. Tan, M. Zhao, L. Qin, K. Yang, Corrosion and biological performance of biodegradable magnesium alloys mediated by low copper addition and processing, Mater. Sci. Eng. C 93 (2018) 565–581.

[58] Z. Geng, L. Ji, Z. Li, J. Wang, H. He, Z. Cui, X. Yang, C. Liu, Nano-needle strontium-substituted apatite coating enhances osteoporotic osseointegration through promoting osteogenesis and inhibiting osteoclastogenesis, Bioactive Materials 6 (2021) 905–915.

[59] S. Hiromoto, M. Inoue, T. Taguchi, M. Yamane, N. Ohtsu, In vitro and in vivo biocompatibility and corrosion behaviour of a bioabsorbable magnesium alloy coated with octacalcium phosphate and hydroxyapatite, Acta Biomater. 11 (2015) 520–530.

[60] S. Chen, J. Zhang, Y. Chen, S. Zhao, M. Chen, X. Li, M.F. Maitz, J. Wang, N. Huang, Application of phenol/amine copolymerized film modified magnesium alloys: anticorrosion and surface biofunctionalization, ACS Appl. Mater. Interfaces 7 (2015) 24510–24522.

[61] M. Mandal, A.P. Moon, G. Deo, C.L. Mendis, K. Mondal, Corrosion behavior of Mg–2.4Zn alloy micro-alloyed with Ag and Ca, Corrosion Sci. 78 (2014) 172–182.

[62] F. Amerstorfer, S.F. Fischerauer, L. Fischer, J. Eichler, J. Draxler, A. Zitek, M. Meischel, E. Martinelli, T. Kraus, S. Hann, S.E. Stanzl-Tschegg, P.J. Uggowitzer, J.F. Loffler, A.M. Weinberg, T. Prohaska, Long-term in vivo degradation behavior and near-implant distribution of resorbed elements for magnesium alloys WZ21 and ZX50, Acta Biomater. 42 (2016) 440–450.

[63] S. Zhang, X. Zhang, C. Zhao, J. Li, Y. Song, C. Xie, H. Tao, Y. Zhang, Y. He, Y. Jiang, Y. Bian, Research on an Mg–Zn alloy as a degradable biomaterial, Acta Biomater. 6 (2010) 626–640.

[64] J. Wang, H. Jiang, Y. Bi, J.e. Sun, M. Chen, D. Liu, Effects of gas produced by degradation of Mg–Zn–Zr Alloy on cancellous bone tissue, Mater. Sci. Eng. C 55 (2015) 556–561.

[65] F. Witte, N. Hort, C. Vogt, S. Cohen, K.U. Kainer, R. Willumeit, F. Feyerabend, Degradable biomaterials based on magnesium corrosion, Curr. Opin. Solid State Mater. Sci. 12 (2008) 63–72.

[66] G. Song, Control of biodegradation of biocompatable magnesium alloys, Corrosion Sci. 49 (2007) 1696–1701.

[67] J. Kuhlmann, I. Bartsch, E. Willbold, S. Schuchardt, O. Holz, N. Hort, D. Hoche, W. R. Heineman, F. Witte, Fast escape of hydrogen from gas cavities around corroding magnesium implants, Acta Biomater. 9 (2013) 8714–8721.

[68] M. Razavi, M. Fathi, O. Savabi, S.M. Razavi, F. Heidari, M. Manshaei, D. Vashaee, L. Tayebi, In vivo study of nanostructured diopside (CaMgSi2O6) coating on magnesium alloy as biodegradable orthopedic implants, Appl. Surf. Sci. 313 (2014) 60–66.

[69] L. Elkaiam, O. Hakimi, G. Yosafovich-Doitch, S. Ovadia, E. Aghion, Vivo evaluation of Mg–5%Zn–2%Nd alloy as an innovative biodegradable implant material, in: Ann Biomed Eng vol. 48, 2020, pp. 380–392.